Validation of the CrIS Fast Physical NH₃ Retrieval with ground-based FTIR

Enrico Dammers[1], Mark W. Shephard[2], Mathias Palm[3], Karen Cady-Pereira[4], Shannon Capps[5*], Erik Lutsch[6],

Kim Strong[6], James W. Hannigan[7], Ivan Ortega[7], Geoffrey C. Toon[8], Wolfgang Stremme[9], Michel Grutter[9],

Nicholas Jones[10], Dan Smale[11], Jacob Siemons[2], Kevin Hrpcek[12], Denis Tremblay[13], Martijn Schaap[14], Justus

Notholt[3], Jan Willem Erisman[1,15]

1. Cluster Earth and Climate, Department of Earth Sciences, Vrije Universiteit Amsterdam, Amsterdam, the
Netherlands
2. Environment and Climate Change Canada, Toronto, Ontario, Canada
3. Institut für Umweltphysik, University of Bremen, Bremen, Germany
4. Atmospheric and Environmental Research (AER), Lexington, Massachusetts, USA
5. Department of Mechanical Engineering, University of Colorado, Boulder, Colorado, USA
6. Department of Physics, University of Toronto, Toronto, Ontario, Canada
7. NCAR, Boulder, Colorado, United States
8. Jet Propulsion Laboratory, California Institute of Technology, Pasadena, California, USA
9. Centro de Ciencias de la Atmósfera, Universidad Nacional Autónoma de México, Mexico City, Mexico
10. University of Wollongong, Wollongong, Australia
11. National Institute of Water and Atmosphere, Lauder, New Zealand
12. University of Wisconsin-Madison Space Science and Engineering Center (SSEC), Madison, Wisconsin, USA.
13. Science Data Processing, Inc., Laurel, MD, United States
14. TNO Built Environment and Geosciences, Department of Air Quality and Climate, Utrecht, the Netherlands
15. Louis Bolk Institute, Driebergen, the Netherlands
*Now at Civil, Architectural, and Environmental Engineering Department, Drexel University, Philadelphia,

Pennsylvania, USA

Correspondence to: E. Dammers (enrico.dammers@gmail.com)

Abstract

Presented here is the validation of the CrIS Fast Physical Retrieval (CFPR) NH₃ column and profile measurements using ground-based Fourier Transform Infrared (FTIR) observations. We use the total columns and profiles from seven FTIR sites in the Network for the Detection of Atmospheric Composition Change (NDACC) to validate the satellite data products. The overall FTIR and CrIS total columns have a positive correlation of r = 0.77 (N=218) with very little bias (a slope of 1.02). Binning the comparisons by total column amounts, for concentrations larger than 1.0×10^{16} molecules cm^{-2}, i.e. ranging from moderate to polluted conditions, the relative difference is on average ~ 0 - 5% with a standard deviation of 25-50%, which is comparable to the estimated retrieval uncertainties in both CrIS and the FTIR. For the smallest total column range ($<1.0 \times 10^{16}$ molecules cm^{-2}) where there are a large number of observations at or near the CrIS noise level (detection limit) the absolute differences between CrIS and the FTIR total columns show a slight positive column bias. The CrIS and FTIR profile comparisons differences are mostly within the range of the estimated retrieval uncertainties single level retrieved profile values, showing average differences in the range of ~20 to 40%. The CrIS retrievals typically show good vertical sensitivity down into the boundary layer that typically peaks at ~850 hPa (~1.5 km), at this level the median absolute difference is 0.87 (std = ±0.08) ppb, corresponding to a median relative difference of 39% (std = ±2%). Most of the absolute and relative profile comparison differences are in the range of the estimated retrieval uncertainties. At the surface,

42   where CrIS typically has lower sensitivity, it tends to overestimate under low concentrations conditions, and

43   underestimate under higher atmospheric concentration conditions.

1. Introduction

The disruption of the nitrogen cycle by the human creation of reactive nitrogen has created one of the major challenges for humankind (Rockström et al., 2009). Global reactive nitrogen emissions into the air have increased to unsurpassed levels (Fowler et al., 2013) and are currently estimated to be four times larger than pre-industrial levels (Holland et al., 1999). As a consequence the deposition of atmospheric reactive nitrogen has increased causing ecosystems and species loss (Rodhe et al 2002; Dentener et al., 2006; Bobbink et al., 2010). Ammonia (NH_3) as fertilizer is essential for agricultural production and is one of the most important reactive nitrogen species in the biosphere. NH_3 emission, atmospheric transport, and atmospheric deposition are major causes of eutrophication and acidification of soils and water in semi-natural environments (Erisman et al., 2008, 2011). Through reactions with sulphuric acid and nitric acid, ammonium nitrate and ammonium sulphate are formed, which embody up to 50% of the mass of fine mode particulate matter ($PM_{2.5}$) (Seinfeld and Pandis., 1988; Schaap et al., 2004). $PM_{2.5}$ has been associated with various health impacts (Pope et al., 2002; 2009). At the same time, atmospheric aerosols impact global climate directly through their radiative forcing effect and indirectly through the formation of clouds (Adams et al., 2001; Myhre et al., 2013). By fertilizing ecosystems, deposition of NH_3 and other reactive nitrogen compounds also plays a key role in the sequestration of carbon dioxide (Oren et al., 2001).

Despite the significance and impact of NH_3 on the environment and climate, its global distribution and budget are still relatively uncertain (Erisman et al., 2007; Clarisse et al., 2009; Sutton et al., 2013). One of the reasons is that in-situ measuring of atmospheric NH_3 at ambient levels is complex due to the sticky nature and reactivity of the molecule, leading to large uncertainties and/or sampling artefacts with the currently used measuring techniques (von Bobrutzki et al., 2010; Puchalski et al., 2011). Measurements are also very sparse. Currently, observations of NH_3 are mostly available in north-western Europe and central North America, supplemented by a small number of observations made in China (Van Damme et al., 2015b). Furthermore, there is a lack of detailed information on its vertical distribution as only a few dedicated airborne measurements are available (Nowak et al., 2007, 2010; Leen et al., 2013, Whitburn et al., 2015, Shephard et al., 2015). The atmospheric lifetime of NH_3 is rather short, ranging from hours to a few days. In summary, global emission estimates have large uncertainties. Estimates of regional emissions attributed to source types different from the main regions are even more uncertain due to a lack of process knowledge and atmospheric levels (Reis et al., 2009).

Over the last decade the developments of satellite observations of NH_3 from instruments such as the Cross-track Infrared Sounder (CrIS, Shephard and Cady-Pereira, 2015), the Infrared Atmospheric Sounding Interferometer (IASI, Clarisse et al., 2009; Coheur et al., 2009; Van Damme et al., 2014a), the Atmospheric Infrared Sounder (AIRS, Warner et al., 2016), and the Tropospheric Emission Spectrometer (TES, Beer et al., 2008; Shephard et al., 2011) show potential to improve our understanding of the NH_3 distribution. Recent studies show the global distribution of NH_3 measured at a twice daily scale (Van Damme et al., 2014a, Van Damme et al., 2015a) can reveal seasonal cycles and distributions for regions where measurements were unavailable until now. Comparisons of these observations to surface observations and model simulations, show underestimations of the modelled NH_3 concentration levels, pointing to underestimated regional and national emissions (Clarisse et al.,

84 2009; Shephard et al., 2011; Heald et al., 2012; Nowak et al., 2012; Zhu et al., 2013; Van Damme et al., 2014b;

85 Lonsdale et al., 2016; Schiferl et al., 2014, 2016; Zondlo et al., 2016). However, the overall quality of the

86 satellite observations is still highly uncertain due to a lack of validation. The few validation studies showed a

87 limited vertical, spatial and or temporal coverage of surface observations to do a proper uncertainty analysis

88 (Van Damme et al., 2015b; Shephard et al., 2015; Sun et al., 2015). A recent study by Dammers et al. (2016a)

89 explored the use of Fourier transform infrared (FTIR-NH_3, Dammers et al., 2015) observations to evaluate the

90 uncertainty of the IASI-NH_3 total column product. The study showed the good performance of the IASI-LUT

91 (Look up table, LUT, Van Damme et al., 2014a) retrieval with a high correlation (r ~ 0.8), but indicated an

92 underestimation of around 30% due to potential assumptions of the shape of the vertical profile (Whitburn et al.,

93 2016, IASI-NN (Neural Network, NN)), uncertainty in spectral line parameters and assumptions on the

94 distributions of interfering species. The study showed the potential of using FTIR observations to validate

95 satellite observations of NH_3, but also stressed the challenges of validating retrievals that do not provide the

96 vertical measurement sensitivity, such as the IASI-LUT retrieval. Since no IASI satellite averaging kernels are

97 provided for each retrieval, and thus no information is available on the vertical sensitivity and/or vertical

98 distribution of each separate observation, it is hard to determine the cause of the discrepancies between both

99 observations.

100

101 The new CrIS Fast Physical Retrieval (Shephard and Cady-Pereira, 2015) uses an optimal estimation retrieval

102 approach that provides the information content and the vertical sensitivity (derived from the averaging kernels,

103 for more details see Shephard and Cady-Pereira, 2015), and robust and straightforward retrieval error estimates

104 based on retrieval input parameters. The quality of the retrieval has so far not been thoroughly examined against

105 other observations. Shephard and Cady-Pereira (2015) used Observing System Simulation Experiment (OSSE)

106 studies to evaluate the initial performance of the CrIS NH_3 retrieval, and report a small positive retrieval bias of

107 6% with a standard deviation of ±20% (ranging from ±12 to ±30% over the vertical profile). Note that no

108 potential systematic errors were included in these OSSE simulations. Their study also shows good qualitative

109 comparisons with the Tropospheric Emission Spectrometer (TES) satellite (Shephard et al., 2011) and the

110 ground-level in situ Quantum Cascade-Laser (QCL) observations (Miller et al., 2014) for a case study over the

111 Central Valley in CA, USA, during the DISCOVER-AQ campaign. However, currently there has not been an

112 extensive validation of the CrIS NH_3 retrievals using direct comparisons against vertical profile observations. In

113 this study we will provide both direct comparisons of the CrIS retrieved profiles against ground-based FTIR

114 observations, and comparisons of CrIS total column values against the FTIR and IASI.

115

2. Methods

2.1   The CrIS Fast Physical Retrieval

CrIS was launched in late October 2011 on board the Suomi NPP platform. CrIS follows a sun-synchronous orbit with a daytime overpass time at 13:30 local time (ascending) and a night time equator overpass at 1:30. The instrument scans along a 2200 km swath using a 3 x 3 array of circular shaped pixels with a diameter of 14 km at nadir for each pixel, becoming larger ovals away from nadir. In this study we use the NH_3 retrieval as described by Shephard and Cady-Pereira (2015). The retrieval is based on an optimal estimation approach (Rodgers, 2000) that minimizes the differences between CrIS spectral radiances and simulated forward model radiances computed from the Optimal Spectral Sampling (OSS) OSS-CrIS (Moncet et al., 2008), which is built from the well-validated Line-By-Line Radiative Transfer Model (LBLRTM) (Clough et al., 2005; Shephard et al., 2009; Alvarado et al., 2013) and uses the HITRAN database (Rothman et al., 2014) for its spectral lines. The fast computational speed of OSS facilitates the operational production of CrIS retrieved (Level 2) products using an optimal estimation retrieval approach (Moncet et al., 2005). The CrIS OSS radiative transfer forward model computes the spectrum for the full CrIS LW band, at the CrIS spectral resolution of 0.625 cm^{-1} (Tobin, 2012), thus the complete NH_3 spectral band (near 10 μm) is available for the retrievals. However, only a small number of micro windows are selected for the CrIS retrievals to both maximize the information content and minimize the influence of errors. Worden et al., (2004) provides an example of a robust spectral region selection process that takes into consideration both the estimated errors (i.e. instrument noise, spectroscopy errors, interfering species, etc.) and the associated information content in order to select the optimal spectral regions for the retrieval. The a-priori profiles selection for the optimal estimation retrievals follows the Tropospheric Emission Spectrometer (TES) retrieval algorithm (Shephard et al., 2011); Based on the relative NH_3 signal in the spectra the a-priori is selected from one of three possible profiles representing unpolluted, moderate, and polluted conditions. The initial guess profiles are also selected from these three potential profiles.

An advantage of using an optimal estimation retrieval approach is that averaging kernels (sensitivity to the true state) and the estimated errors of the retrieved parameter are computed in a robust and straight-forward manner (for more details see Shephard and Cady-Pereira, 2015). The total satellite retrieved parameter error is expressed as the sum of the smoothing error (due to unresolved fine structure in the profile), the measurement error (random instrument noise in the radiance spectrum propagated to the retrieval parameter), and systematic errors from uncertainties in the non-retrieved forward model parameters and cross-state errors propagated from retrieval-to-retrieval (i.e. major interfering species such as H_2O, CO_2, and O_3) (Worden et al., 2004). As of yet we have not included error estimates for the systematic errors. The CrIS smoothing error is computed, but since in these FTIR comparison results we apply the FTIR observational operator (which accounts for the smoothing error), the smoothing error contribution is not included in the CrIS errors reported in the comparisons. Thus,

150 only the measurement errors are reported for observations used here; these errors can thus be considered the

151 lower limit on the total estimated CrIS retrieval error.

152 Figure 1 shows an example of CrIS NH$_3$ observations surrounding one of the ground-based FTIR instruments.

153 This is a composite map of all days in Bremen with observations in 2015. This figure shows the wide spread

154 elevated amounts of NH$_3$ across north-western Germany as observed by CrIS.

155
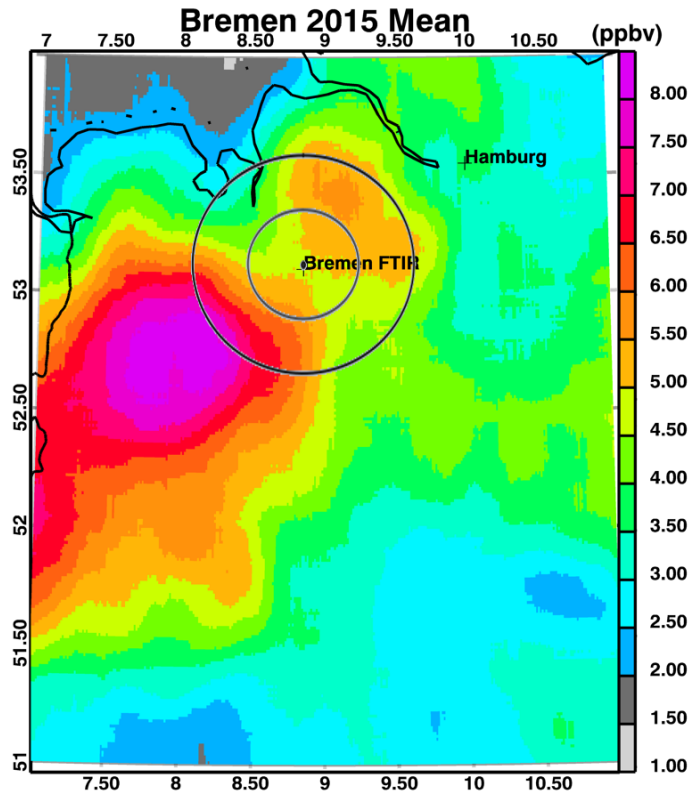
156 **Figure 1.** Annual mean of the CrIS retrieved NH$_3$ surface VMR values around the Bremen FTIR site for 2015.

157 The two circles show the collocation area when for radii of 25 and 50 km.

158 Since the goal of this analysis is to evaluate the CrIS retrievals that provide information beyond the a-priori, we

159 only performed comparisons when the CrIS spectrum presents a NH$_3$ signal. We also focused our efforts on

160 FTIR stations that have FTIR observations with total columns larger than 5 x 10^{15} molecules cm^{-2}(~1-2 ppb

161 surface VMR). This restriction does mean that a number of sites of the FTIR-NH$_3$ dataset will not be used. For

162 comparability of this study to the results of the IASI-LUT evaluation in an earlier study by Dammers et al.,

163 (2016a) we include a short paragraph on the performance of the IASI-LUT and the more recent IASI-NN

164 product when applying similar constraints.

165 **2.2   FTIR-NH$_3$ retrieval**

166 The FTIR-NH$_3$ product used in this study is similar to the set described in Dammers et al. (2016a) and is based

167 on the retrieval methodology described by Dammers et al. (2015). The retrieval methodology uses two spectral

168 micro-windows whose spectral width depends on the NH$_3$ background concentration determined for the

169 observation stations and location (wider window for stations with background concentrations less than one ppb).

170 NH$_3$ is retrieved by fitting the spectral lines in the two micro-windows MW1 [930.32-931.32 cm^{-1} or wide:

171 929.40-931.40 cm^{-1}] and MW2 [962.70-970.00 cm^{-1} or wide: 962.10-970.00 cm^{-1}. An optimal estimation

172 approach (Rodgers et al., 2000) is used, implemented in the SFIT4 algorithm (Pougatchev et al., 1995; Hase et

173 al., 2004, 2006). There are a number of species that can interfere to some extent in both windows, with the

174 major species being H$_2$O, CO$_2$ and O$_3$ and the minor species N$_2$O, HNO$_3$, CFC-12, and SF$_6$. The HITRAN 2012

175 database (Rothman et al., 2014) is used for the spectral lines. A further set of spectroscopic line parameter

176 adjustments are added for CO$_2$ taken from the ATMOS database (Brown et al., 1996) as well as a set of pseudo-

177 lines for the broad absorptions by the CFC-12 and SF$_6$ molecules (created by NASA-JPL, G.C. Toon,

178 http://mark4sun.jpl.nasa.gov/pseudo.html). The NH$_3$ a-priori profiles are based on balloon measurements (Toon

179 et al., 1999) and refitted to match the local surface concentrations (depending on the station either measured or

180 estimated by model results). For the interfering species a-priori profiles we use the Whole Atmosphere

181 Community Climate Model (WACCM, Chang et al., 2008, v3548). The estimated errors in the FTIR-NH$_3$

182 retrievals are in the order of ~30% (Dammers et al., 2015) with the uncertainties in the NH$_3$ line spectroscopy

183 being the most important contributor. Based on the data requirements in section 2.1, a set of seven stations is

184 used (Table 1). For all sites except Wollongong in Australia we use the basic narrow spectral windows. For

185 Wollongong the wide spectral windows are used. For a more detailed description of each of the stations see the

186 publications listed in Table 1 or Dammers et al. (2016a).

187 **Table 1.** The location, longitudinal and latitudinal position, altitude above sea level, and type of instrument for

188 each of the FTIR sites used in this study. In addition, a reference is given to a detailed site description, when

189 available.

Station	Lon (degrees)	Lat (degrees)	Altitude (m.a.s.l)	FTIR instrument	Reference
Bremen, Germany	8.85E	53.10N	27	Bruker 125 HR	Velazco et al., 2007
Toronto, Canada	79.60W	43.66N	174	ABB Bomem DA8	Wiacek et al., 2007 Lutsch et al., 2016
Boulder, United States	105.26W	39.99N	1634	Bruker 120 HR	
Pasadena, United States	118.17W	34.20N	350	MkIV_JPL	
Mexico City, Mexico	99.18W	19.33N	2260	Bruker Vertex 80	Bezanilla et al., 2014
Wollongong, Australia	150.88E	34.41S	30	Bruker 125 HR	
Lauder, New Zealand	169.68E	45.04S	370	Bruker 120 HR	Morgenstern et al., 2012

190

191 **2.3 IASI-NH$_3$**

192 The CrIS retrieval will also be compared with corresponding IASI/FTIR retrievals using results from a previous

193 study by Dammers et al. (2016a). Both the IASI-LUT (Van Damme et al., 2014a) and the IASI-NN (Neural

194 Networks, Whitburn et al., 2016) retrievals from observations by the IASI instrument aboard MetOp-A will be

195 used. A short description of both IASI retrievals is provided here, for a more in-depth description, see the

196 respective publications by Van Damme et al. (2014a) and Whitburn et al. (2016). The IASI instrument on board

197 the MetOp-A platform is in a sun-synchronous orbit and has a daytime overpass at around 9:30 local solar time

198 and a night time overpass at around 21:30. The instrument has a circular footprint of about 12 km diameter for

199 nadir viewing angles with of nadir observations along a swath of 2100 km. Both IASI retrievals are based on the

200 calculation of a dimensionless spectral index called the Hyperspectral Range Index (HRI) (Van Damme et al.,

201 2014a). The HRI is representative of the amount of NH$_3$ in the measured column. The IASI-LUT retrieval

202 makes a direct conversion of the HRI to a total column density with the use of a look-up-table (LUT). The LUT

203 is created using a large number of simulations for a wide range of atmospheric conditions which links the
204 Thermal Contrast (TC, the difference between the air temperature at 1.5 km altitude and the temperature of the
205 Earth surface) and the HRI to a NH_3 total column density. The retrieval includes a retrieval error based on the
206 uncertainties in the initial HRI and TC parameters. The more recent IASI-NN retrieval (Whitburn et al., 2016)
207 follows similar steps but it makes use of a neural network. The neural network combines the complete
208 temperature, humidity and pressure profiles for a better representation of the state of the atmosphere. At the
209 same time the retrieval error estimate is improved by including error terms for the uncertainty in the profile
210 shape, and the full temperature and water vapour profiles. The IASI-NN version uses the fixed profiles that were
211 described by Van Damme et al., (2014) but allows for the use of third party profiles to improve the
212 representation of the NH_3 atmospheric profile. The IASI-LUT and IASI-NN retrievals have both been
213 previously compared with FTIR observations (Dammers et al., 2016a, Dammers et al., 2016b). They compared
214 reasonably well with correlations around r=0.8 for a set of FTIR stations, with an underestimation of around
215 30% that depends slightly on the magnitude of total column amounts, with the IASI-NN performing slightly
216 better.
217
218 **2.4   Data criteria & quality**
219 NH_3 concentrations show large variations both in space and time as the result of the large heterogeneity in
220 emission strengths due to spatially variable sources and drivers such as meteorology and land use (Sutton et al.,
221 2013). This high variability poses challenges in matching ground-based point observations made by FTIR
222 observations with CrIS downward-looking satellite measurements which have a 14-km nadir footprint. For the
223 pairing of the measurement data we apply data selection criteria similar to that described in Dammers et al.
224 (2016a) and summarized in Table 2. To minimize the impact of the heterogeneity of the sources, we choose a
225 maximum of 50 km between the centre points of the CrIS observations and the FTIR site location. To diminish
226 the effect of temporal differences between the FTIR and CrIS observations a maximum time difference of 90
227 minutes is used. Topographical effects are reduced by choosing a maximum altitude difference of 300 m at any
228 point between the FTIR site location and the centre point of the satellite pixel location. The altitude differences
229 are calculated using the Space Shuttle Radar Topography Mission Global product at 3 arc-second resolution
230 (SRTMGL3, Farr et al., 2007). To ensure the data quality of CrIS-NH_3 retrieval for Version 1.0, a small number
231 of outliers with a maximum retrieved concentration above 200 ppb (at any point in the profile) were removed
232 from the comparison dataset. While potentially a surface NH_3 value of 200 ppb (and above) would be possible
233 (i.e. downwind of forest fires), it is highly unlikely to occur over the entire footprint of the satellite instrument.
234 Moreover, after inspecting these data points, they seem to be affected by numerical issues in the fitting
235 procedure (possibly due to interfering species). As we are interested in validating the CrIS observational
236 information (not just a-priori information), we only select comparisons that contain some information from the
237 satellite (degrees of freedom for signal (DOFS) $\geq$ 0.1). Do note that on average the observations have a DOFS
238 between 0.9 and 1.1. The DOFS > 0.1 filter only removes some of the outliers at the lower end. No explicit filter
239 is applied to account for clouds; however, clouds will implicitly be accounted for by the quality control as CrIS
240 will not measure a NH_3 signal (e.g. DOFS < 0.1) below optically thick clouds (e.g. cloud optical depth >~1). In
241 addition, the CrIS observations are matched with FTIR observations taken only during clear-sky conditions,
242 which mostly eliminates influence from cloud cover. Finally, the high signal to noise ratios (SNR) of the CrIS

243   instrument, allows it to retrieve NH_3 from a thermal contrast approaching 0 K during daytime observations

244   (Clarisse et al., 2010). Given this, we decided not to apply a thermal contrast filter to the CrIS data. No

245   additional filters are applied to the FTIR observations beyond the clear-sky requirement.

246

247   For both IASI retrievals, we use the same observation selection criteria as described in Dammers et al. (2016a).

248   The set of criteria is similar to those used here for the CrIS observations. Observations from both IASI retrievals

249   are matched using the overpass time, and longitudinal and latitudinal positions. For comparability with CrIS a

250   spatial difference limit of 50 km limit was used, instead of the 25 km spatial limit used in the previous study.

251   Furthermore we apply the thermal contrast (> 12K, difference between the temperatures at 1.5 km and the

252   surface) and Earth skin temperature criteria to the IASI observations to match the previous study.

253

254   **Table 2. Coincidence criteria and quality flags applied to the satellite and FTIR data. The third through**

255   **fifth columns show the number of observations remaining after each subsequent data criteria step and**

256   **the number of possible combinations between the CrIS and FTIR observations. The first set of numbers**

257   **indicate the number of CrIS observations within a 1°x 1° degree square surrounding the FTIR site.**

Filter	Data Criteria	Nr. Obs.		
		FTIR	CrIS	Combinations
CrIS		15661	25855	
Temporal sampling difference	Max 90 min	1576	13959	112179
Spatial sampling difference	Max 50 km	1514	3134	22869
Elevation difference	Max 300 m	1505	1642	9713
Quality flag	DOFS ≥ 0.1	1433	1453	8579

258

259   **2.5   Observational Operator Application**

260

261   To account for the vertical sensitivity and the influence of the a-priori profiles of both retrievals we apply the

262   observational operator (averaging kernel and a-priori of the retrieval) of the FTIR retrieval to the CrIS retrieved

263   profiles. The CrIS observations are matched to each individual FTIR observation in time and space following

264   the matching criteria. The FTIR averaging kernels, a-priori profiles, and retrieved profiles are first mapped to

265   the CrIS pressure levels (fixed pressure grid, layers are made smaller or cut off for observations above elevation

266   to fit the fixed pressure grid). Following Rodgers and Connor (2003) and Calisesi et al. (2005) this results in the

267   mapped FTIR averaging kernel, A_{ftir}^{mapped}, the mapped FTIR apriori, $x_{ftir}^{mapped,apriori}$, and the mapped FTIR

268   retrieved profile, x_{ftir}^{mapped}. Then we apply the FTIR observational operator to the CrIS observations using **eq.**

269   **(1)**.

270     $$\hat{x}_{CrIS} = x_{ftir}^{mapped,apriori} + A_{ftir}^{mapped}(x_{CrIS} - x_{ftir}^{mapped,apriori})$$ **(1)**

271     $$\widehat{\Delta x}_{abs} = \hat{x}_{CrIS} - x_{ftir}^{mapped}$$ **(2)**

272     $$\widehat{\Delta x}_{rel} = (\hat{x}_{CrIS} - x_{ftir}^{mapped})/(0.5\, x_{ftir}^{mapped} + 0.5\, \hat{x}_{CrIS})$$ **(3)**

273   where $x_{ftir}^{apriori}$ is the FTIR a-priori profile, x_{ftir}^{mapped} is the interpolated FTIR profile, A_{ftir}^{mapped} is the FTIR

274   averaging kernel, and $\hat{x}_{CrIS}$ is the smoothed CrIS profile.

275

276 The CrIS smoothed profile $\hat{x}_{CrIS}$ calculated from equation (1) provides an estimate of the FTIR retrieval applied

277 to the CrIS satellite profile. Next we evaluate both total column and profile measurements.

278 For the first validation step, following Dammers et al. (2016a), who evaluated the IASI-LUT (Van Damme et

279 al., 2014a) product, we sum the individual profile ($\hat{x}_{CrIS}$) to obtain a column total to compare to the FTIR total

280 columns. This step gives the opportunity to evaluate the CrIS retrieval in a similar manner as was done with the

281 IASI-LUT retrieval. If multiple FTIR observations match a single CrIS overpass we also average those together

282 into a single value as well as each matching averaged CrIS observation. Therefore, it is possible to have multiple

283 FTIR observations, each with multiple CrIS observations all averaged into a single matching representative

284 observation. For the profile comparison this averaging is not performed to keep as much detail available as

285 possible. An important point to make is that this approach assumes that the FTIR retrieval gives a better

286 representation of the truth. While this may be true, the FTIR retrieval will not match the truth completely. For

287 readability we assume that the FTIR retrieval indeed gives a better representation of the truth, and in the next

288 sections will describe the case in which we apply the FTIR observational operator to the CrIS values. For the

289 tenacious reader we included a similar set of results in the appendix, using the CrIS observational operator

290 instead of the FTIR observational operator, as the assumption of the FTIR being truth is not exactly right.

291

292 **3. Results and discussion**

293 **3.1 Total column comparison**

294
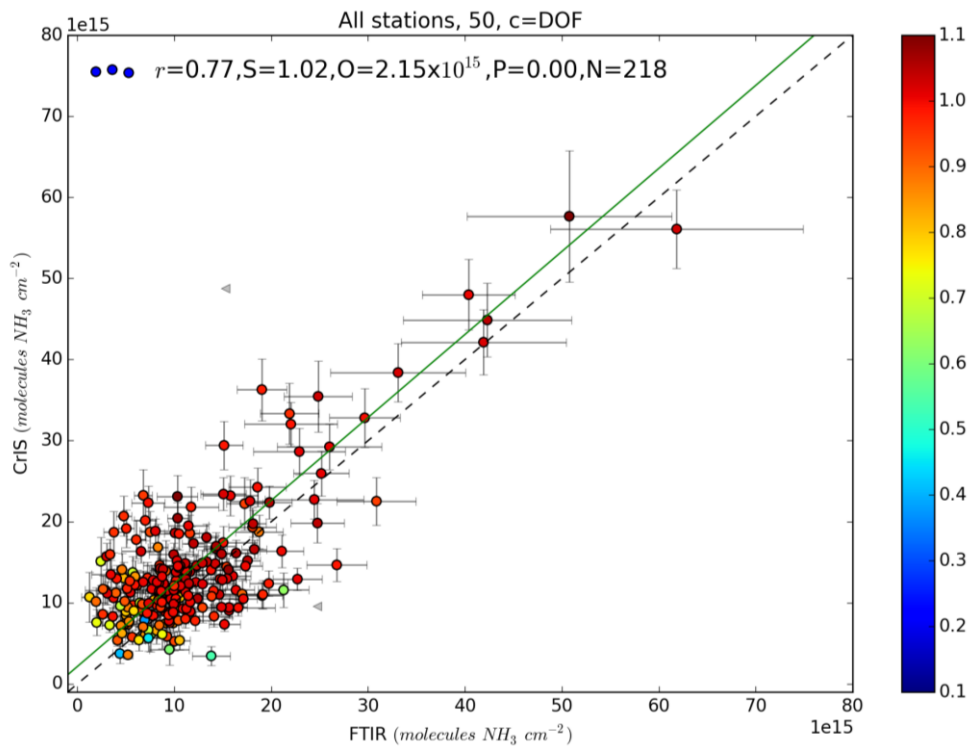
295 **Figure 2.** Correlation between the FTIR and CrIS total columns using the coincident data from all measurement

296 sites. The horizontal and vertical bars show the total estimated error on each FTIR and CrIS observation. The

297 colouring on the scatter indicates the mean DOF of each the CrIS coincident data. The trend line shows the

298 results of the regression analysis.

299

300   The total columns are averaged as explained in Section 2.4 to show a direct comparison of FTIR measurements

301   with CrIS observations in Figure 2. A three sigma outlier filter was applied to calculate the regression statistics.

302   The filtered outliers are displayed in grey, and may be caused by low information content (DOFS) and terrain

303   characteristics. For the regression we used the reduced major axis regression (Bevington and Robinson, 1992),

304   accounting for possible errors both in the x and y values. There is an overall agreement with a correlation of r =

305   0.77 (P < 0.01, N = 218) and a slope of 1.02 (+- 0.05). At the lower range of values the CrIS column totals are

306   higher than the observed FTIR values. Possibly the CrIS retrieval overestimates due to the low sensitivity to low

307   concentrations. Without the sensitivity the retrieval will find a value more closely to the a-priori, which may be

308   too high. Figure 3 shows the comparisons at each station. When the comparisons are broken down by station

309   (Figure 3), the correlation varies from site to site, from a minimum of 0.28 in Mexico City (possibly due to

310   retrieval errors associated with the highly irregular terrain) to a maximum of 0.84 in Bremen. Similarly to

311   Mexico City the comparison also shows an increase in scatter for Pasadena, where the FTIR site is also located

312   on a hill. In Toronto and Bremen there is good agreement when NH_3 is elevated (> 20 x 10^{15} molecules cm^{-2}),

313   and low bias in the CrIS total columns for intermediate values (between 10 and 20 x 10^{15} molecules cm^{-2})

314   except for the outlying observation in Bremen, which is marked as an outlier by our three sigma filter used for

315   Figure 2. In Wollongong, there is less agreement between the instruments. There are two comparisons with large

316   CrIS to FTIR ratios while most of the other comparisons also show a bias for CrIS. For both cases the bias can

317   be explained by the heterogeneity of the ammonia concentrations in the surrounding regions. The two outlying

318   observations were made during the end of November, 2012, which coincides with wild fires in the surrounding

319   region. Furthermore the Wollongong site is located coastally, which will increase the occurrences where one

320   instrument observes clean air from the ocean while the other observes inland air masses.

321
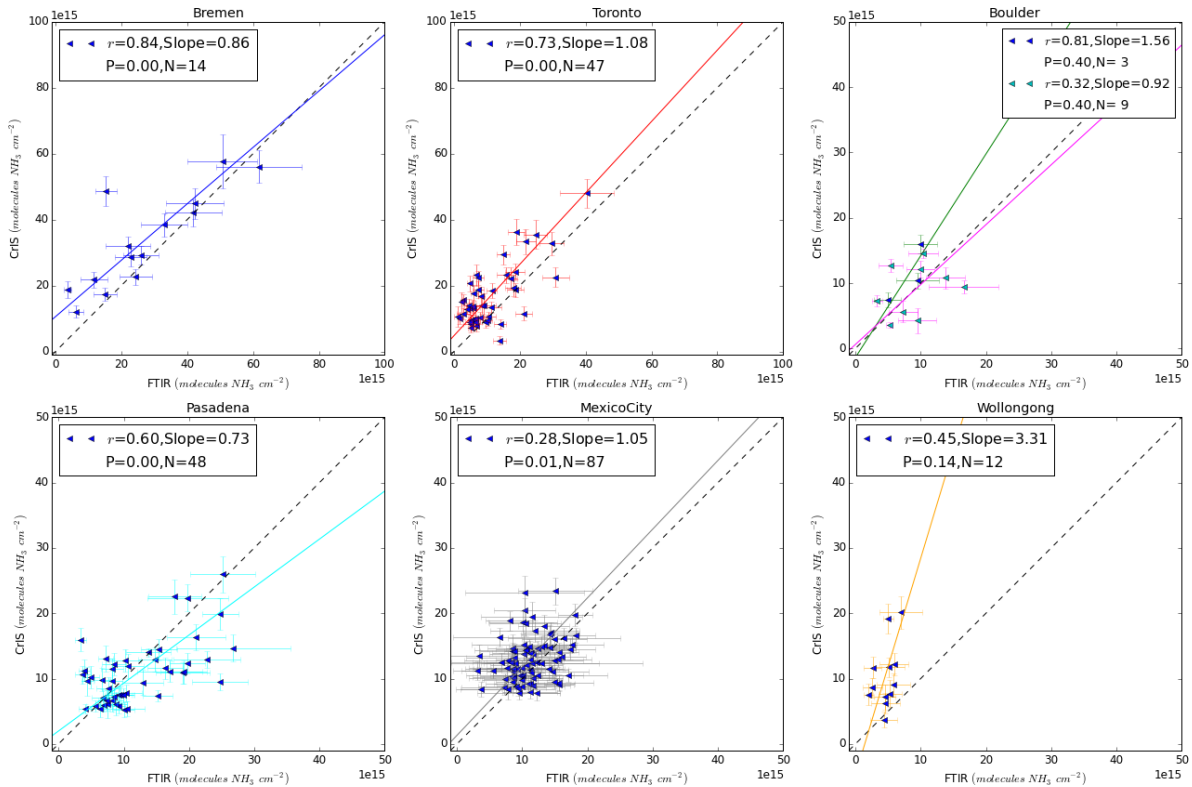
322   **Figure 3.** FTIR vs CrIS comparison scatter plots showing the correlations for each of the individual stations,

323   with estimates error plotted for each value. The trend lines show the individual regression results. Note the

324 different ranges on the x and y axis. The results for the Boulder (green line) and Lauder (pink line) sites are

325 shown in the same panel.

326

327
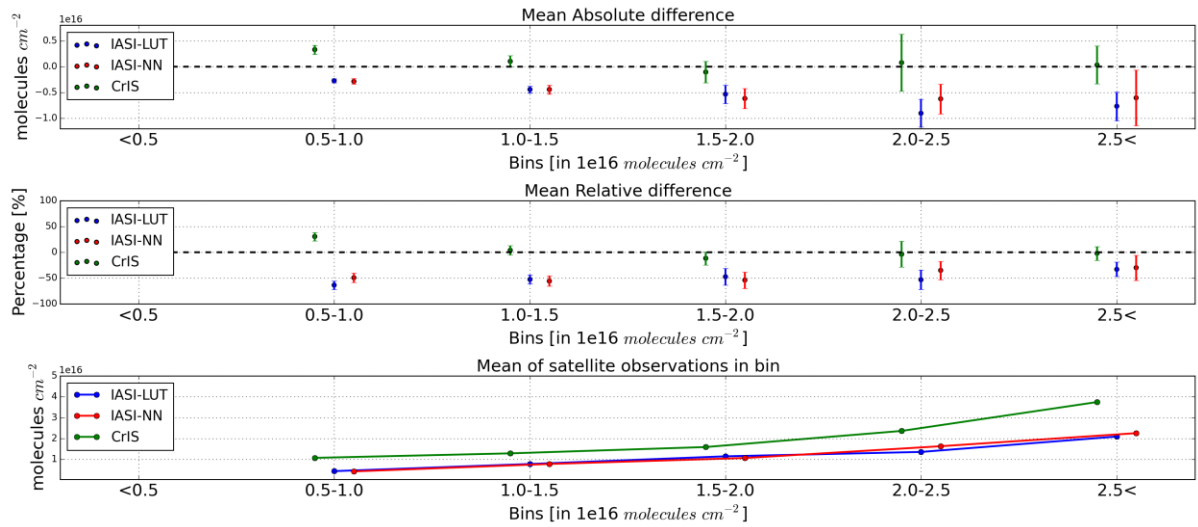
328 **Figure 4.** Plots of the mean absolute and relative differences between CrIS and IASI, as a function of NH_3 total

329 column. Observations are separated into bins of total columns. The upper panel shows the mean absolute

330 difference (MD). The middle panel shows the mean relative difference. The bars in these top two panels show

331 the 95 % confidence interval for each value. The bottom panel shows the mean of the observations in each bin.

332 The number of observations in each set is shown in the bottom panel.

333

334 The mean absolute (MD) and relative difference (MRD) are calculated following equation 4 and equation 5;

335 $$MRD = \frac{1}{N}\sum_{i=1}^{N}\frac{(CrIS\ column_i - FTIR\ column_i)\ x\ 100}{0.5*FTIR\ column_i + 0.5*CrIS\ column_i}$$ **(4)**

336 $$MD = \frac{1}{N}\sum_{i=1}^{N}(CrIS\ column_i - FTIR\ column_i)$$ **(5)**

337 with N being the number of observations.

338

339 **Table 3.** Results of the total column comparisons of the FTIR to CrIS, FTIR to IASI-LUT and FTIR to IASI-

340 NN. N is the number of averaged total columns, MD is the mean difference [10^{15} molecules cm^{-2}], MRD is the

341 mean relative difference [frac, in %]. Take note that the combined value N does not add up with all the separate

342 sites as observations have been included for FTIR total columns > 5 x 10^{15} molecules cm^{-2}.

Retrieval	Column total range in molecules cm^{-2}	N	MD in 10^{15} (1σ)	MRD in % (1σ)	FTIR mean in 10^{15} (1σ)
CrIS-NH3	< 10.0 x 10^{15}	93	3.3 (4.1)	30.2 (38.0)	7.5 (1.5)
CrIS-NH3	>= 10.0 x 10^{15}	109	0.4 (5.3)	-1.39 (34.4)	16.7 (8.5)
IASI-LUT	< 10.0 x 10^{15}	229	-2.7 (3.0)	-63.6 (62.6)	7.1 (1.4)
IASI-LUT	>= 10.0 x 10^{15}	156	-5.1 (4.2)	-50.2 (43.6)	14.8 (6.7)
IASI-NN	< 10.0 x 10^{15}	212	-2.2 (3.6)	-57.0 (68.7)	7.1 (1.4)
IASI-NN	>= 10.0 x 10^{15}	156	-5.0 (5.1)	-52.5 (49.7)	14.8 (6.7)

343

344 We evaluate the data by subdividing the comparisons over a set of total column bins as a function of the FTIR

345 total column value of each individual observation. The bins (with a range of 5 x10^{15} to 25 x10^{15} molecules cm^{-2}

346 with iterations steps of 5 x 10^{15} molecules cm^{-2}) give a better representation of the performance of the retrieval

347 as it shows the influence of the retrieval as a function of magnitude of the total column densities. The results of

348 these total column comparisons are presented in Figure 4. Table 3 summarizes the results for each of the FTIR

349 to satellite column comparisons into two total column bins, which splits the comparisons between smaller and

350 larger than 10 x 10^{15} molecules cm^{-2}. A few combinations of the IASI-NN and FTIR retrievals have a small

351 denominator value that causes problems in the calculation of the MRD. A three sigma outlier filter based on the

352 relative difference is applied to remove these outliers (<10 x 10^{15} molecules cm^{-2}, only the IASI-NN set). The

353 statistical values are not given separately by site because of the low number of matching observations for a

354 number of the sites.

355

356 The CrIS/FTIR comparison results show a large positive difference in both the absolute (MD) and relative

357 (MRD) for the smallest bin, (5.0-10.0 x 10^{15} molecules cm^{-2}). The rest of the CrIS/FTIR comparison bins with

358 NH_3 values > 10.0 x 10^{15} agree very well with a nearly constant bias (MD) around zero, and a standard

359 deviation of the order of 5.0 x 10^{15} that slightly dips below zero in the middle bin. The standard deviation over

360 these bins is also more or less constant, and the weak dependence on the number of observations in each bin

361 indicates that most of the effect is coming from the random error on the observations. The relative difference

362 becomes systematically smaller with increasing column total amounts, and tend towards zero with a standard

363 deviation ~25-50%, which is on the order of the reported estimated errors of the FTIR retrieval (Dammers et al,

364 2015).

365

366 For a comparison against previous reported satellite results, we included both the IASI-LUT (Van Damme et al.,

367 2014a) and the IASI-NN (Whitburn et al., 2016) comparisons against the FTIR observations. To put the results

368 of this study into perspective of the IASI-LUT and IASI-NN products we added Figure A1 to the Appendix,

369 which shows the total column comparison for both products. Both IASI products show similar differences as a

370 function of NH_3 column bins, which is somewhat different from the CrIS/FTIR comparison results. The absolute

371 difference (MD) is mostly negative with the smallest factor for the smallest total column bin, with a difference

372 around -2.5 x 10^{15} (std = ±3.0 x 10^{15}, N = 229) molecules cm^{-2} that slowly increases as a function of the total

373 column. However, the relative difference (MRD) is at its maximum for the smaller bin with a difference of the

374 order -50% (std = ±~50%, N=229) which decreases to ~ -10-25% (std = ±25%) with increasing bin value. For

375 both the IASI-NN and IASI-LUT retrievals we find an underestimation of the total columns, which originates

376 mostly from a large systematic error in combination with more randomly distributed error sources such as the

377 instrument noise and interfering species, which is similar to results reported earlier for IASI-LUT (Dammers et

378 al., 2016b).

379

380 A number of factors, besides the earlier reported FTIR uncertainties, can explain the differences between the

381 FTIR and CrIS measurements. The small positive bias found for CrIS points to a small systematic error. The

382 higher SNR, from both the low radiometric noise and high spectral resolution, enables it to resolve smaller

383 gradients in the retrieved spectra, which potentially can provide greater vertical information and detect smaller

384 column amounts (lower detection limit). This could explain the larger MRD and MD CrIS differences at the

385 lower end of the total column range. However, a number of standalone tests with the FTIR retrieval showed

386 only a minor increase in the total column following a decrease in spectral resolution, which indicates that the

387 spectral resolution itself is not enough to explain the difference.

388

389 **3.2   Profile Comparison**

390 The CrIS satellite and FTIR retrieved profiles are matched using the criteria specified above in Table 2 and

391 compared. It is possible for a CrIS observation to be included multiple times in the comparison as there can be

392 more than one FTIR observation per day, and /or, the possibility of multiple satellite overpasses that match a

393 single FTIR observation.

394 **A representative profile example**

395 An example of the profile information contained in a representative CrIS and FTIR profile is shown in Fig. 5.

396 Although the vertical sensitivity and distribution of NH_3 differs per station this is a fairly representative. The

397 FTIR usually has a somewhat larger DOFS in the order of 1.0-2.0, mostly depending on the concentration of

398 NH_3, compared to the CrIS total of ~1 DOFS. Figure 5a shows an unsmoothed FTIR averaging kernel [vmr vmr^{-1}

399] of a typical FTIR observation. The averaging kernel (AVK) peaks between the surface and ~850 hPa, which is

400 typical for most observations. In specific cases with plumes overpassing the site, the averaging kernel peak is at

401 a higher altitude matching the location of the NH_3 plume. The CrIS averaging kernel (Fig. 5b) usually has a

402 maximum somewhere in between 680-850 hPa depending on the local conditions. This particular observation

403 has a maximum near the surface, an indication of a day with high thermal contrast. Both the FTIR and CrIS

404 concentration profiles have a maximum at the surface with a continuous decrease that mostly matches the a-

405 priori profile in shape following the low DOFS. This is visible for layers at the lower pressures (higher altitudes)

406 where the FTIR and CrIS a-priori and retrieved volume mixing ratios become similar and near zero. The

407 absolute difference between the FTIR and CrIS profiles can be calculated by applying the FTIR observational

408 operator to the CrIS profile, as we described in section 2.5. The largest absolute difference (Fig. 5d) is found at

409 the surface, which is also generally where the largest absolute NH_3 values occur. The FTIR smoothed relative

410 difference (red, striped line) peaks at the pressure where the sensitivity of the CrIS retrieval is highest (~55%),

411 which goes down to ~20-30% for the higher altitude and surface pressure layers. Overall the retrievals agree

412 with most of the difference explained by the estimated errors of the individual retrievals. For an illustration of

413 the systematic and random errors on the FTIR and CrIS profiles shown in Fig 5, see the figures in the appendix:

414 for the FTIR error profile see Fig. A2 (absolute error) and A3 (relative error) and for the CrIS measurement

415 error profile see Fig. A4. Please note that we only show the diagonal error covariance values for each of the

416 errors, which is common practice. The total column of our example profile is ~20 x 10^{15} molecules cm^{-2} which

417 is a slightly larger value than average. The total random error is < 10% for each of the layers, mostly dominated

418 by the measurement error, which is somewhat smaller than average (Dammers et al., 2015) following the larger

419 NH_3 VMR. A similar value is found for the CrIS measurement error with most layers showing an error < 10%.

420 The FTIR systematic error is around ~10% near the surface and grows to a larger 40% for the layers between

421 900 – 750 hPa. The error is mostly due to the errors in the NH_3 spectroscopy (Dammers et al., 2015). The shape

422 of the relative difference between the FTIR and CrIS closely follows the shape systematic error on the FTIR

423 profile pointing to that error as the main cause of difference.
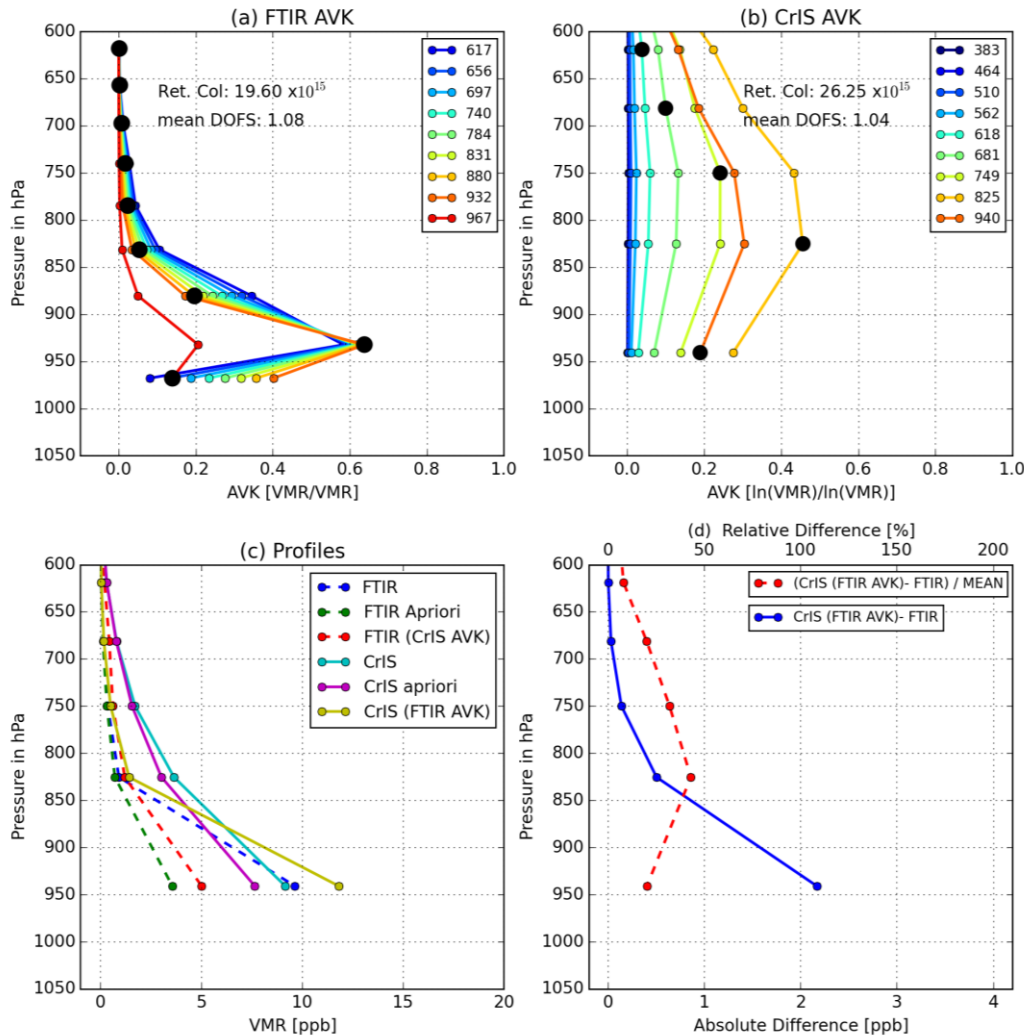
Figure 5. Example of the NH$_3$ profile comparison for an FTIR profile matched with a CrIS profile measured around the Pasadena site. With (a) the FTIR averaging kernel, (b) the CrIS averaging kernel. For both averaging kernels the black dots show the matrices diagonal values. Panel (c) shows the retrieved profiles of both FTIR (blue) and CrIS (cyan) with the FTIR values mapped to the CrIS pressure layers. Also shown are the FTIR a-priori (green), the CrIS a-priori (purple), the CrIS retrieved profile smoothed with the FTIR averaging kernel [CrIS (FTIR AVK)] (yellow) and the FTIR profile smoothed with the CrIS averaging kernel [FTIR (CrIS AVK)](red). In panel (d), the blue line is the absolute difference between the FTIR profile (blue, panel (c)) and the CrIS profile smoothed with the FTIR averaging kernel (Yellow, panel (c)) with the red line the corresponding relative difference.

All paired data

In Fig. 6 all the individual site comparisons were merged. The Mexico City site was left out of this figure because of the large number of observations in combination with a difference in pressure grid due to the high altitude of the city obscured the overall analysis and biased the results towards the results of one station. Similar to the single profile example, the FTIR profile peaks near the surface for most observations, slowly going towards zero with decreasing pressure. Compared to the representative profile example a number of differences

440   emerge. A number of FTIR observations peak further above the surface and are shown as outliers, which drag

441   the mean further away from the median values. The combined CrIS profile in Fig. 6 shows a similar behaviour,

442   although for the lowest pressure layer it has a lower median and mean compared to the layer above. The

443   difference between Fig. 5 and Fig. 6e derives mostly from the number of observations used in the boxplot, many

444   with weak sensitivity at the surface. Similar to the single profile example in Fig. 5, the FTIR averaging kernels

445   in Fig. 6c on average peak near or just above the surface (with the diagonal elements of the AVK's shown in the

446   figure). The sensitivity varies a great deal between the observations as shown by the large spread of the

447   individual layers. The CrIS averaging kernels (Fig. 6g) usually peak in the boundary layer around the 779 hPa

448   layer with the 2 surrounding layers having somewhat similar values. The instrument is less sensitive to the

449   surface layer as is demonstrated by the large decrease in the AVK near the surface, but this varies depending on

450   the local conditions. We find the largest absolute differences in the lower three layers, as was seen in the

451   example in Fig. 5, although the differences decrease downwards rather than increase. The relative difference

452   shows a similar shape to Fig 5. Overall both retrievals show agreement. The relative differences in the single

453   level retrieved profile values in Fig. 6h show an average difference in the range of ~20 to 40% with the 25th and

454   75th percentiles at around 60-80%, which partially follows from our large range of concentrations. The absolute

455   difference shows an average difference in the range of -0.66 to 0.87 ppb around the peak sensitivity levels of the

456   CrIS observations (681 to 849 hPa). The lower number of surface observations follow from the fact that only the

457   Bremen site is located at an altitude low enough for the CrIS retrieval to provide a result at this pressure level.

458   Due to this difference in retrieval layering, the remaining 227 observations mostly follow from matching

459   observations in Bremen, which is located in a region of significant NH_3 emissions.

460

461
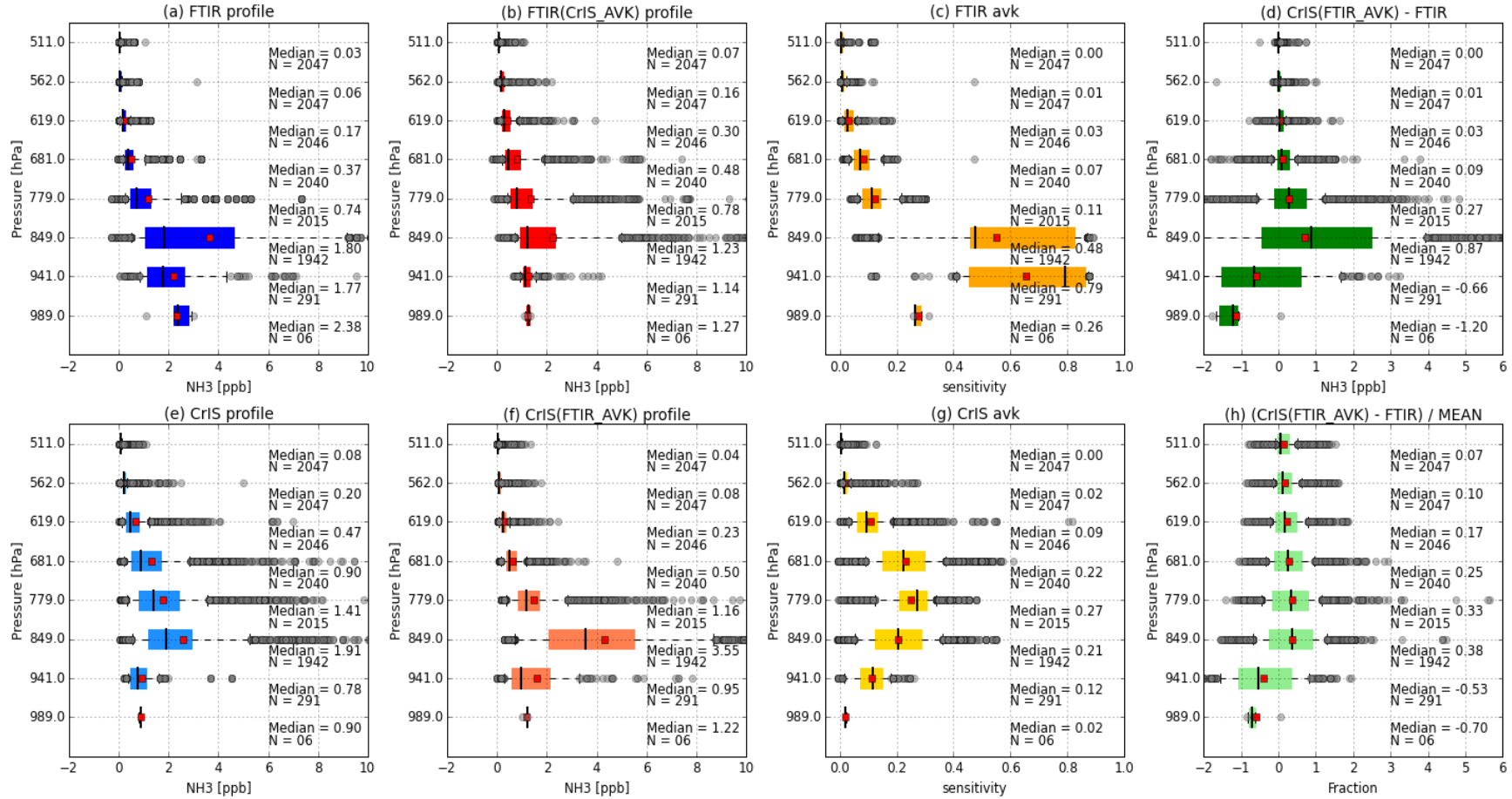
Figure 6. Profile comparison for all stations combined. Observations are combined following pressure "bins", i.e. the midpoints of the CrIS pressure grid. Subplot (a) shows the mean profiles of the FTIR (blue), (b) the profiles of FTIR with the CrIS averaging kernel applied to it (red), (c) the FTIR averaging kernel diagonal values, and (d) shows the absolute difference [VMR] between profiles (f) and (a). The second row shows the CrIS mean profile in (e), (f) the profiles of CrIS with the FTIR averaging kernel applied, (g) the CrIS averaging kernel diagonal values, (h) the relative difference [Fraction] between the profiles in (f) and (a). Each of the boxes edges are the 25th and 75th percentiles, the black lines in each box is the median, the red square is the mean, the whiskers are the 10th and 90th percentiles, and the grey circles are the outlier values outside the whiskers.
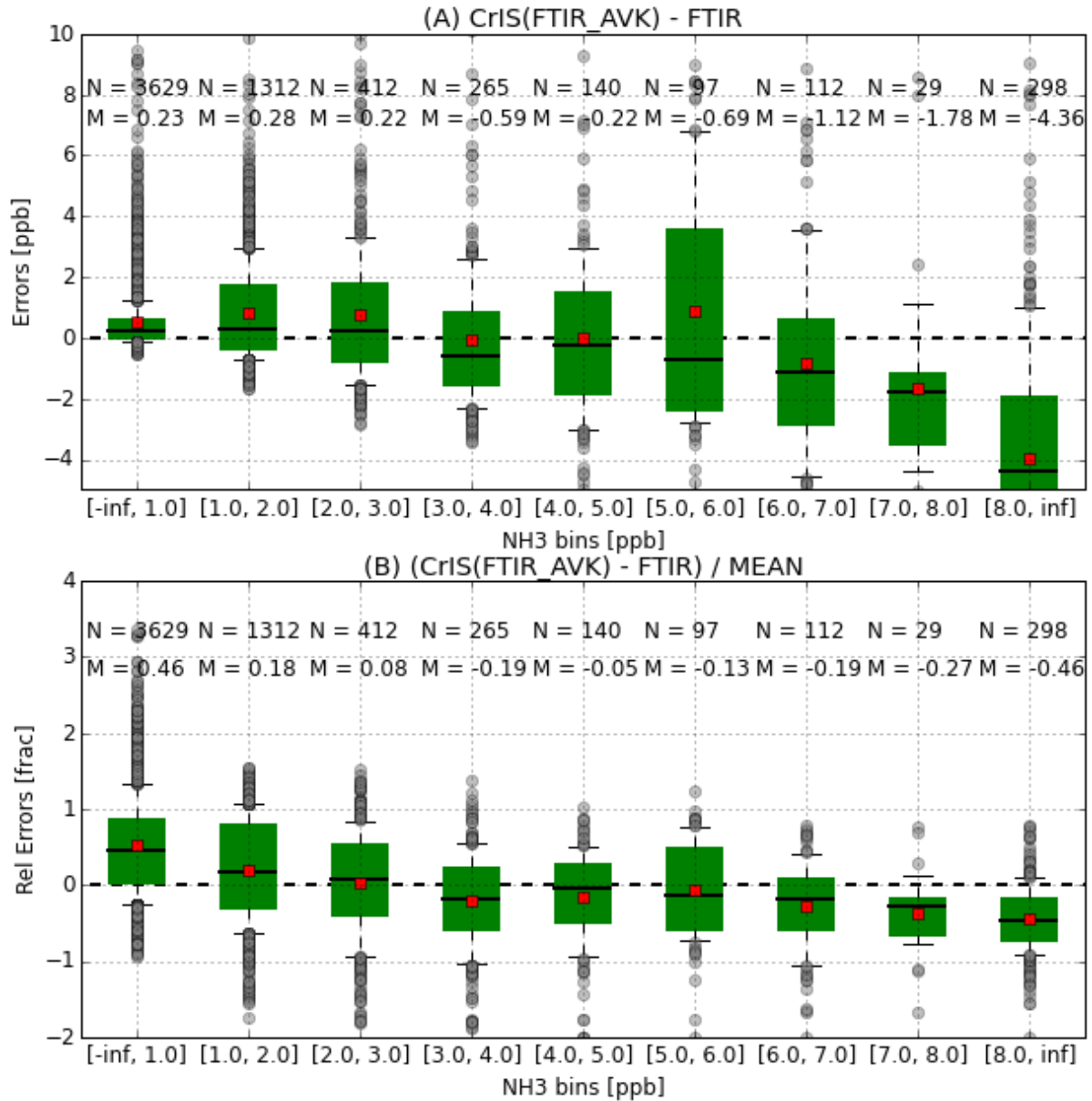
Figure 7. Summary of the absolute and relative actual error as a function of the VMR of NH_3 in the individual FTIR layers. The box edges are the 25th and 75th percentiles, the black line in the box is the median, the red square is the mean, the whiskers are the 10th and 90th percentiles, and the grey circles are the outlier values outside the whiskers. Only observations with a pressure greater than 650 hPa are used. The top panel shows the absolute difference for each VMR bin, the bottom panel shows the relative difference for each VMR bin.

The switch between negative and positive values in the absolute difference (see Fig. 6d), occurs in the two lowest layers dominated by the Bremen observations and provides insight into the relation between absolute differences as function of retrieved concentration. Fig. 7 shows a summary of the differences as a function of the individual NH_3 VMR layer amounts. As seen before in the column comparison, e.g. Fig 2 and 4, the CrIS retrieval gives larger total columns than the FTIR retrieval for the small values of VMR. For increasing VMRs, this slowly tends to a negative absolute difference with a relative difference in the range of 20-30%. However, note that the number of compared values in these high VMR bins are by far lower than in the first three bins

482 leading to relatively less effect in the total column and merged VMR figures (Figs. 2 and 6) from these high

483 VMR bins. We now combine the results of Figs. 6 and 7 into Figure 8 to create a set of subplots showing the

484 difference between both retrieved profiles as a function of the maximum VMR of each retrieved FTIR profile.

485 For the layers with pressure less than 681 hPa we generally find agreement, which is expected but not very

486 meaningful, since there is not much NH_3 (and thus sensitivity) in these layers and any differences are smoothed

487 out by the application of the observational operator. The relative differences for these layers all lie around ~0-

488 20%. For the lowest two VMR bins we find again that CrIS gives larger results than the FTIR, around the CrIS

489 sensitivity peak in the layer centred around 849 hPa, and to a lesser extent in the layer below. At these VMR

490 levels (< 2 ppb) the NH_3 signal approaches the spectral noise of the CrIS measurement, making the retrievals

491 more uncertain. The switch lies around 2-3 ppb where the difference in the SNR between the instruments

492 becomes less of an issue. Also easily observed is the relation between the concentration and the absolute and

493 relative differences. This can be explained by the difference in sensitivity of the instruments, and the

494 measurement noise of both instruments. For the largest VMR bin [> 4.0 ppb] we find that CrIS is biased for the

495 four lowest layers. Differences are largest in the surface layer where only a few observations are available,

496 almost all from the Bremen site. Most of these CrIS observations have a peak satellite sensitivity at a higher

497 altitude than the FTIR. Assuming that most of the NH_3 can be found directly near the surface, with the

498 concentration dropping off with a sharp gradient as a function of altitude, it is likely that these concentrations

499 are not directly observed by the satellite but are observed by the FTIR instruments. This difference in sensitivity

500 should be at least partially removed by the application of the observational operator but not completely, due to

501 the intrinsic differences between both retrievals. The CrIS retrieval uses one of three available a-priori profiles,

502 which is chosen following a selection based on the strength of NH_3 signature in the spectra. The three a-priori

503 profiles (unpolluted, moderately polluted and polluted) are different in both shape and concentrations. Out of the

504 entire set of 2047 combinations used in Fig. 8, only six are of the not polluted a priori category. About 1/3 of the

505 remaining observations use the polluted a-priori, which has a sharper peak near the surface (see Fig. 5c),

506 compared to the moderately polluted profile, which is used by 2/3s of the CrIS retrievals shown in this work.

507 Based on the results as a function of retrieved VMR (as measured with the FTIR so not a perfect restriction), it

508 is possible that the sharper peak at the surface as well as the low a-priori concentrations are restricting the

509 retrieval. The dependence of the differences on VMR can also possibly follow from uncertainties in the line

510 spectroscopy. In the lower troposphere there is a large gradient in pressure and temperature and the impact of

511 any uncertainty in the line spectroscopy is greatly enhanced. Even for a day with large thermal contrast and NH_3

512 concentrations (e.g. Fig 5.), the difference between both the CrIS and FTIR retrievals was dominated by the line

513 spectroscopy. This effect is further enhanced by the higher spectral resolution and reduced instrument noise of

514 the FTIR instrument, which potentially makes it more able to resolve the line shapes.

515

516
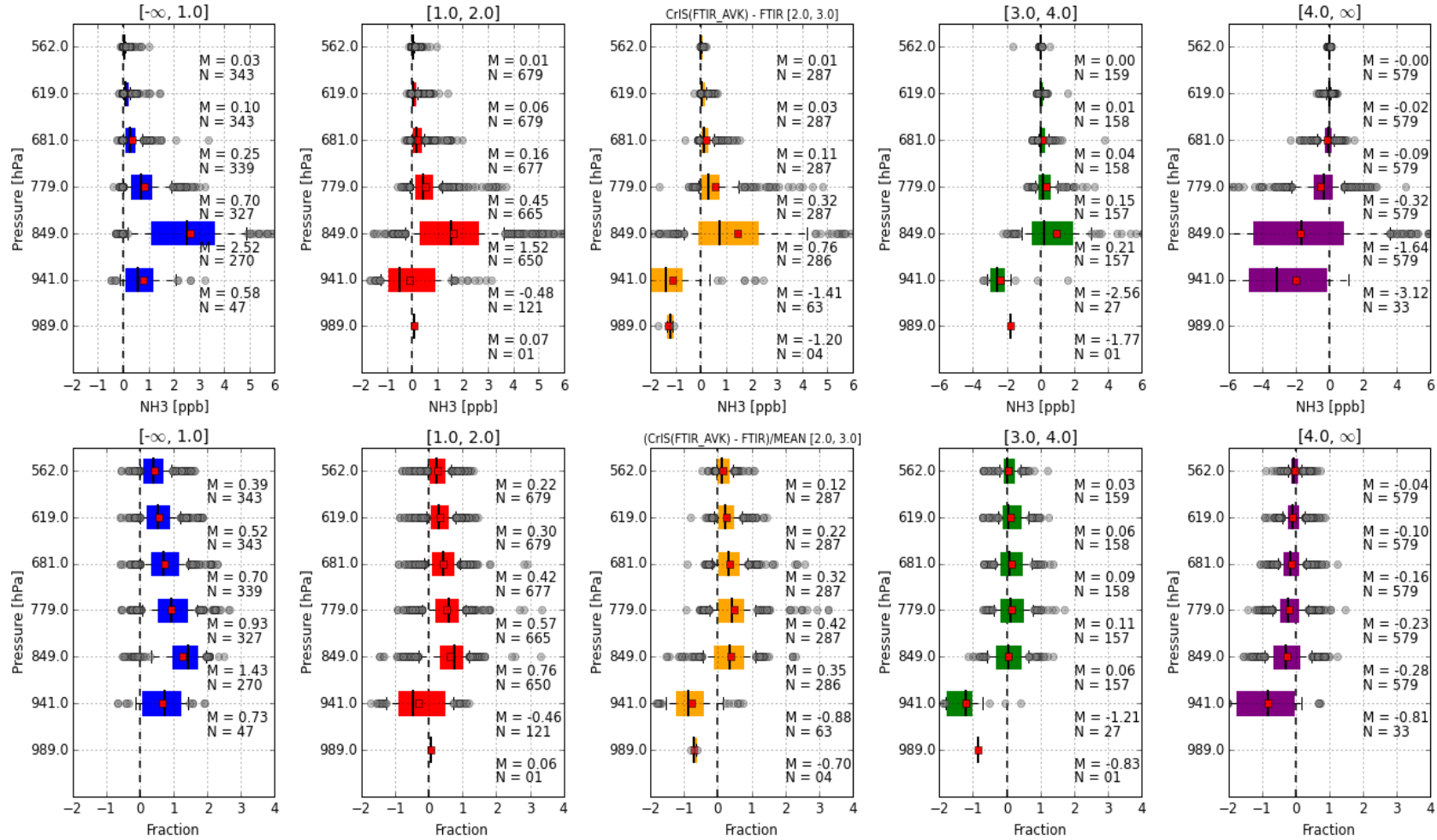
Figure 8. Summary of differences as a function of maximum volume mixing ratio (VMR). The maximum VMR of each FTIR profiles is used for the classification. Absolute (Top row) and relative profile differences (bottom row) following the FTIR and CrIS (FTIR AVK applied) profiles. Observations are following pressure layers, i.e. the midpoints of the CrIS pressure grid. The box edges are the 25th and 75th percentiles, the black line in the box is the median, the red square is the mean, the whiskers are the 10th and 90th percentiles, and the grey circles are the outlier values outside the whiskers.

522 To summarise, the overall differences between both retrievals are quite small, except for the lowest layers in the
523 NH$_3$ profile where CrIS has less sensitivity. The differences mostly follow the errors as estimated by the FTIR
524 retrieval and further effort should focus on the estimated errors and uncertainties. A way to improve the
525 validation would be to add a third set of measurements with a better capability to vertically resolve NH$_3$
526 concentrations from the surface up to ~750 hPa (i.e. the first 2500 m). One way to do this properly is probably
527 by using airplane observations that could measure a spiral around the FTIR path coinciding with a CrIS
528 overpass. The addition of the third set of observations would improve our capabilities to validate the satellite
529 and FTIR retrievals and point out which retrieval specifically is causing the absolute and relative differences at
530 each of the altitudes.
531
532 **4. Conclusions**
533
534 Here we presented the first validation of the CrIS-NH$_3$ product using ground-based FTIR-NH$_3$ observations. The
535 total column comparison shows that both retrievals have a correlation of R = 0.77 (P < 0.01, N = 218) and
536 almost no bias with an overall slope of 1.02 (std = ±0.05). For the individual stations we find varying levels of
537 agreement mostly limited by the small range of NH$_3$ total columns. For FTIR total columns > 10 x 10^{15}
538 molecules cm^{-2} the CrIS and FTIR observations are in agreement with only a small bias of 0.4 (std = ± 5.3) x
539 10^{15} molecules cm^{-2}, and a relative difference 4.57 (std = ± 35.8) %. In the smaller total column range the CrIS
540 retrieval shows a positive bias with larger relative differences 49.0 (std = ± 62.6) % that mostly seems to follow
541 from observations near the CrIS detection limit. The results of the comparison between the FTIR and the IASI-
542 NN and IASI-LUT retrievals, are comparable to those found in earlier studies. Both IASI products showed
543 smaller total column values compared to the FTIR, with a MRD ~-35- -40%. On average, the CrIS retrieval has
544 one piece of information, while the FTIR retrieval shows a bit more vertical information with DOFS in the range
545 of 1-2. The NH$_3$ profile comparison shows similar results, with a small mean negative difference between the
546 CrIS and FTIR profiles for the surface layer and a positive difference for the layers above the surface layer. The
547 relative and absolute differences in the retrieved profiles can be explained by the estimated errors of the
548 individual retrievals. Two causes of uncertainty stand out with the NH$_3$ line spectroscopy being the biggest
549 factor, showing errors of up to 40% in the profile example. The second factor is the signal-to-noise ratio of both
550 instruments which depends on the VMR: under large NH$_3$ concentrations, the FTIR uncertainty in the signal is
551 in the range of 10%; for measurements with small NH$_3$ concentrations this greatly increases. Future work should
552 focus on improvements to the NH$_3$ line spectroscopy to reduce the uncertainty coming from this error source.
553 Furthermore an increased effort is needed to acquire coincident measurements with the FTIR instruments during
554 satellite overpasses as a dedicated validation effort will greatly enhance the number of available observations.
555 Furthermore, a third type of observations measuring the vertical distribution of NH$_3$ could be used to compare
556 with both the FTIR and CrIS retrievals and further constrain the differences. These observations could be
557 provided by an airborne instrument flying spirals around an FTIR site during a satellite overpass.
558

5. Data availability

FTIR-NH$_3$ data (Dammers et al., 2015) can be made available on request (M. Palm, Institut für Umweltphysik, University of Bremen, Bremen, Germany). The CrIS-FRP-NH$_3$ science grade (non-operational) data products used in this study can be made available on request (M. W. Shephard, Environment and Climate Change Canada, Toronto, Ontario, Canada).The IASI-NH$_3$ product is freely available at http://www.pole-ether.fr/etherTypo/index.php?id=1700&L=1 (Van Damme et al., 2015a).

Appendix A.
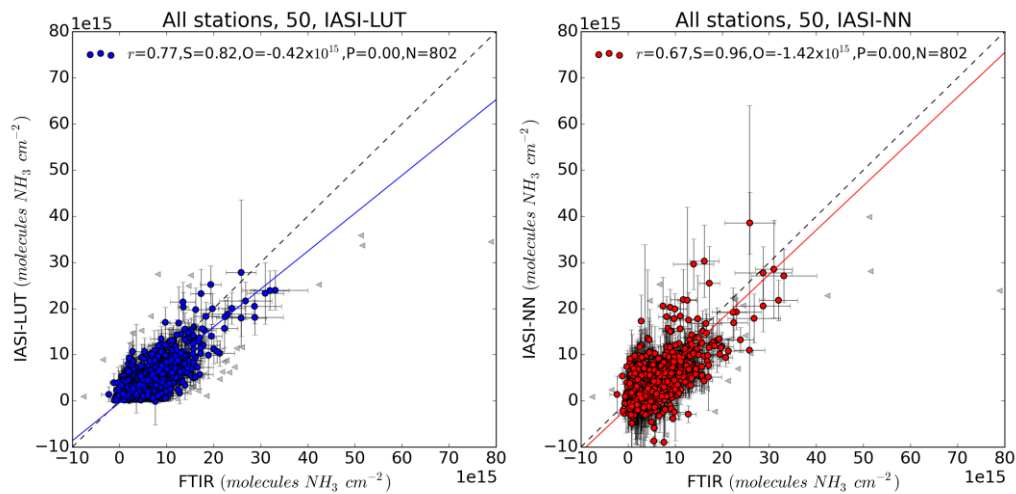
Figure A1. Correlation between the FTIR and the IASI-LUT (left, blue) and IASI-NN (right, red) total columns using the coincident data from all measurement sites. The horizontal and vertical bars show the total estimated error on each FTIR and CrIS observation. A three sigma outlier filter was applied to the IASI-LUT dataset and the same observations were removed from the IASI-NN set. Contrary to the earlier study by Dammers et al., (2016a) no thermal contrast filter was applied to the dataset.

573
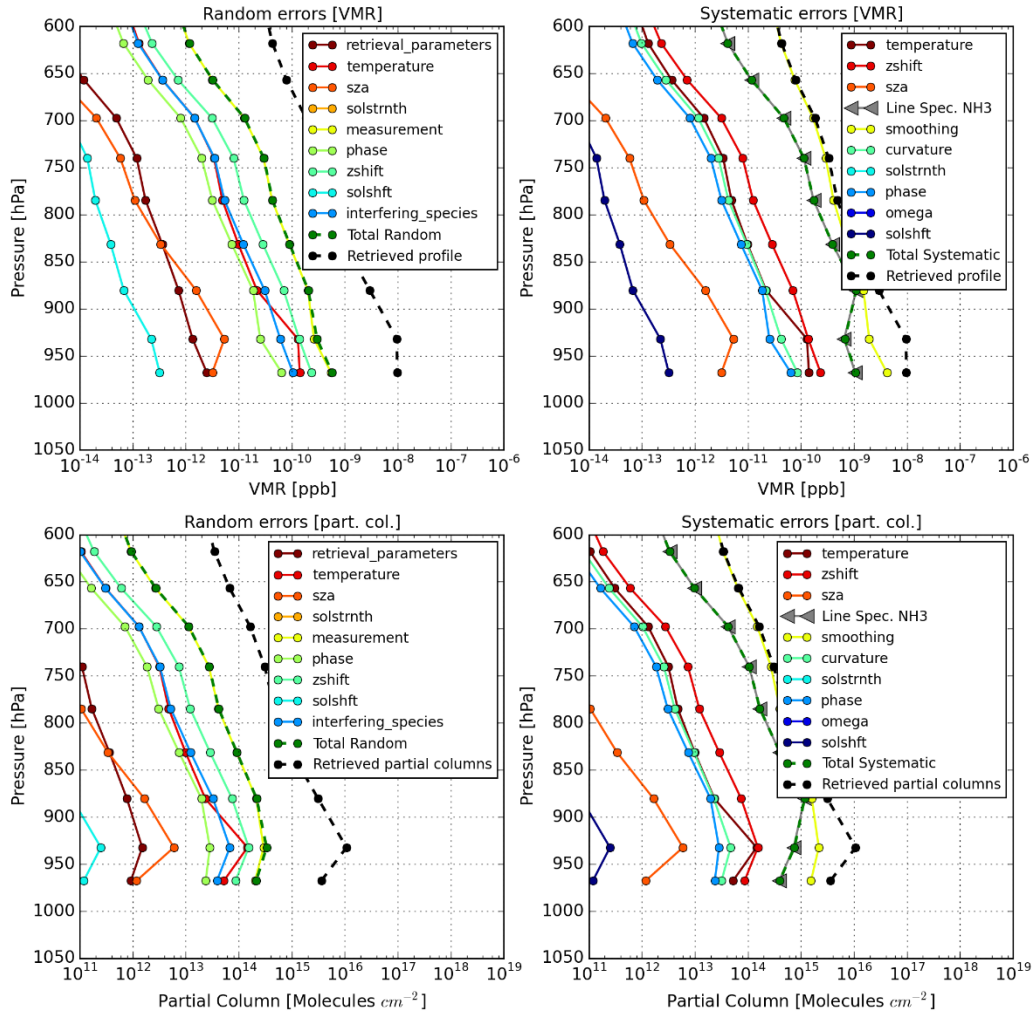
574   **Figure A2.** Error profiles for each of the error terms. The left panels show the Random errors, the right panels

575   the Systematic errors. The top two panels show the error in VMR. The bottom panels show the errors in partial

576   column layers [molecules cm^{-2}]. (See Figure A3 for the same figure but with the errors relative to the final VMR

577   and partial columns per layer)

578
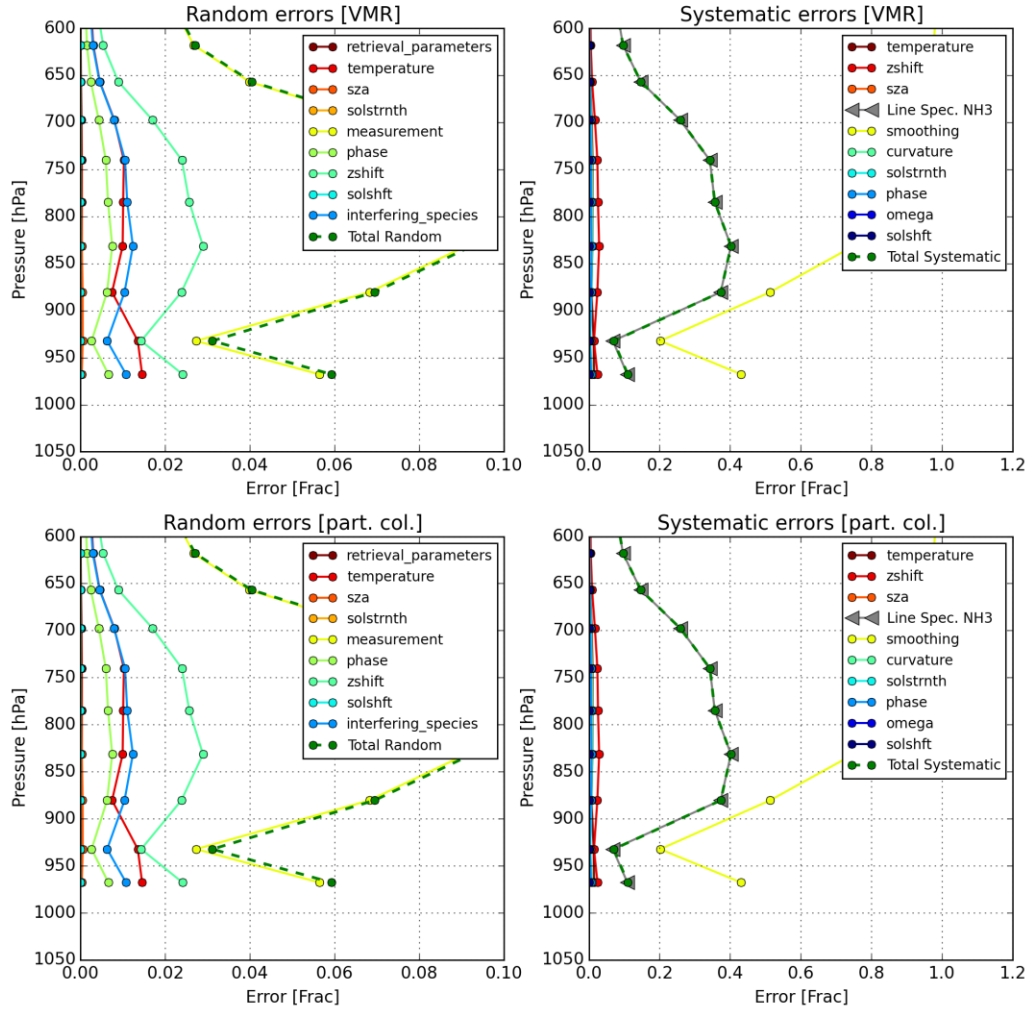
579 **Figure A3.** Relative error profiles for each of the error terms. The left panels show the Random errors, right

580 panels the Systematic errors. All four panels show the error in a fraction of the original unit used in Figure A2.

581 (See Figure A2 for the same figure but with the absolute errors)

582

583
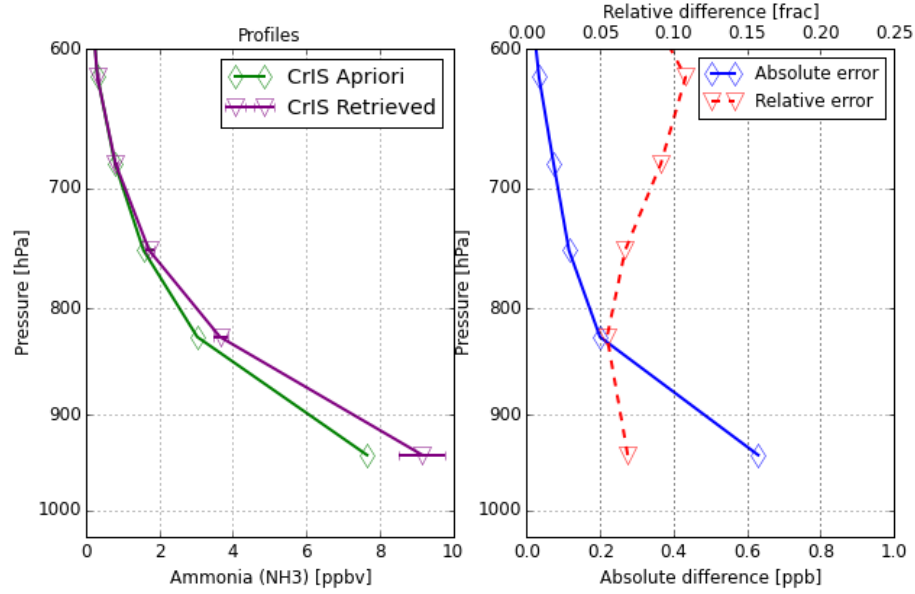
Figure A4. CrIS-NH$_3$ relative and absolute error profile. The left plot shows the retrieved and a-priori profiles similar to the profiles shown in Figure 5c. The right panel shows the measurement error on the CrIS retrieved profile, with the blue line the absolute value and red line the value relative to the retrieved profile.

587

588
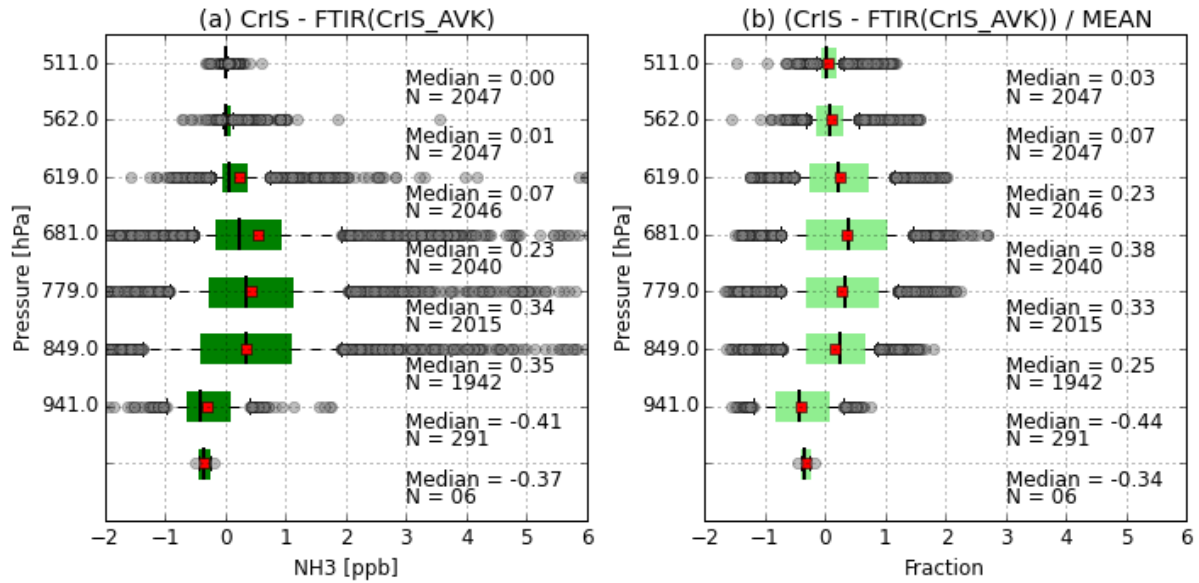
Fig A5. Profile comparison for all stations combined. Observations are combined following pressure "bins", i.e. the midpoints of the CrIS pressure grid. Panel (a) shows the absolute difference [VMR] between profiles (f) and (a). Panel (b) shows the relative difference [Fraction] between the profiles in (Fig 6e) and (Fig 6b). Each of the boxes edges are the 25th and 75th percentiles, the black lines in each box is the median, the red square is the mean, the whiskers are the 10th and 90th percentiles, and the grey circles are the outlier values outside the whiskers.

595

596
597 **Fig A6.** Summary of the absolute and relative actual error as a function of the VMR of NH₃ in the individual
598 FTIR layers. The box edges are the 25th and 75th percentiles, the black line in the box is the median, the red
599 square is the mean, the whiskers are the 10th and 90th percentiles, and the grey circles are the outlier values
600 outside the whiskers. Only observations with a pressure greater than 650 hPa are used. The top panel shows the
601 absolute difference for each VMR bin, the bottom panel shows the relative difference for each VMR bin.
602
603
604

Fig A7. Summary of actual errors as a function of VMR. The maximum VMR of each FTIR profiles is used for the classification. Absolute (Top row) and relative profile differences (bottom row) following the FTIR (CrIS AVK applied) and CrIS profiles. Observations are following pressure layers, i.e. the midpoints of the CrIS pressure grid. The box edges are the 25th and 75th percentiles, the black line in the box is the median, the red square is the mean, the whiskers are the 10th and 90th percentiles, and the grey circles are the outlier values outside the whiskers.

Acknowledgements

This work is part of the research programme GO/12-36, which is financed by the Netherlands Organisation for Scientific Research (NWO). This work was also funded at AER through a NASA funded (contract: NNH15CM65C). We would like to acknowledge the University of Wisconsin-Madison Space Science and Engineering Center Atmosphere SIPS team sponsored under NASA contract NNG15HZ38C for providing us with the CrIS level 1 and 2 input data, in particular Liam Gumley. We would also like to thank Andre Wehe (AER) for developing the CrIS download and extraction software. The IASI-LUT and IASI-NN were obtained from the atmospheric spectroscopy group at ULB (Spectroscopie de l'Atmosphère, Service de Chimie Quantique et Photophysique, Université Libre de Bruxelles, Brussels, Belgium) and we would like to thank Simon Whitburn, Martin Van Damme, Lieven Clarisse and Pierre Francois Coheur for their help and contributions. Part of this work was performed at the Jet Propulsion Laboratory, California Institute of Technology, under contract with NASA. The University of Toronto FTIR retrievals were supported by the CAFTON project, funded by the Canadian Space Agency's FAST programme. Measurements were made at the University of Toronto Atmospheric Observatory (TAO), which has been supported by CFCAS, ABB Bomem, CFI, CSA, EC, NSERC, ORDCF, PREA, and the University of Toronto. Funding support in Mexico City was provided by UNAM-DGAPA grants IN107417 & IN112216. A. Bezanilla and B. Herrera participated in the FTIR measurements and M.A. Robles, W. Gutiérrez and M. García are thanked for technical support. We would also like to thank Roy Wichink Kruit and Margreet van Marle for the numerous discussions and valuable input on the subject.

References

Adams, P.J., Seinfeld, J.H., Koch, D., Mickley, L., Jacob, D. (2001), General circulation model assessment of direct radiative forcing by the sulfate-nitrate-ammonium-water inorganic aerosol system, Journal of Geophysical Research Atmospheres, 106 (1), pp. 1097-1111.

Alvarado, M. J., Payne, V. H., Mlawer, E. J., Uymin, G., Shephard, M. W., Cady-Pereira, K. E., Delamere, J. S., and Moncet, J.-L.: Performance of the Line-By-Line Radiative Transfer Model (LBLRTM) for temperature, water vapor, and trace gas retrievals: recent updates evaluated with IASI case studies, Atmos. Chem. Phys., 13, 6687–6711, doi:10.5194/acp-13-6687-2013, 2013

Beer, R., Shephard, M. W., Kulawik, S. S., Clough, S. a., Eldering, A., Bowman, K. W., Sander, S. P., Fisher, B. M., Payne, V. H., Luo, M., Osterman, G. B. and Worden, J. R.: First satellite observations of lower tropospheric ammonia and methanol, Geophys. Res. Lett., 35(9), 1–5, doi:10.1029/2008GL033642, 2008.

Bevington, P. R. and Robinson D. K. (1992) "Data Reduction and Error Analysis for the Physical Sciences, 2nd Ed." pp: 104, and 108-109, McGraw-Hill, New York.

Bezanilla A., Krueger A., Stremme W. and Grutter M. Solar absorption infrared spectroscopic measurements over Mexico City: Methane enhancements. Atmósfera 27(2), 173-183 (2014).

Bobbink, R, Hicks K, Galloway J, Spranger T, Alkemade R, Ashmore M, Bustamante M, Cinderby S, Davidson E, Dentener F, Emmett B, Erisman JW, Fenn M, Gilliam F, Nordin A, Pardo L, De Vries W. Global assessment of nitrogen deposition effects on terrestrial plant diversity: a synthesis, Ecological Applications, 20 (2010), pp. 30–59.

von Bobrutzki, K., Braban, C. F., Famulari, D., Jones, S. K., Blackall, T., Smith, T. E. L., Blom, M., Coe, H., Gallagher, M., Ghalaieny, M., McGillen, M. R., Percival, C. J., Whitehead, J. D., Ellis, R., Murphy, J., Mohacsi,

A., Pogany, A., Junninen, H., Rantanen, S., Sutton, M. A., and Nemitz, E.: Field inter-comparison of eleven atmospheric ammonia measurement techniques, Atmos. Meas. Tech., 3, 91-112, doi:10.5194/amt-3-91-2010, 2010.

Brown, L. R., M. R. Gunson, R. A. Toth, F. W. Irion, C. P. Rinsland, and A. Goldman. "1995 atmospheric trace molecule spectroscopy (ATMOS) linelist."Applied optics 35, no. 16 (1996): 2828-2848.

Calisesi, Y., V. T. Soebijanta, and R. van Oss (2005), Regridding of remote soundings: Formulation and application to ozone profile comparison, J. Geophys. Res., 110, D23306, doi:10.1029/2005JD006122.

Chang, L., Palo, S., Hagan, M., Richter, J., Garcia, R., Riggin, D. and Fritts, D.: Structure of the migrating diurnal tide in the Whole Atmosphere Community Climate Model (WACCM), Advances in Space Research, 41(9), 1398–1407, doi:10.1016/j.asr.2007.03.035, 2008.

Clarisse, Lieven, Cathy Clerbaux, Frank Dentener, Daniel Hurtmans, and Pierre-François Coheur. "Global ammonia distribution derived from infrared satellite observations." Nature Geoscience 2, no. 7 (2009): 479-483.

Clarisse, L., Shephard, M. W., Dentener, F., Hurtmans, D., Cady-Pereira, K., Karagulian, F., Van Damme, M., Clerbaux, C. and Coheur, P.-F.: Satellite monitoring of ammonia: A case study of the San Joaquin Valley, J. Geophys. Res., 115(D13), 1–15, doi:10.1029/2009JD013291, 2010.

Clough, S. A., Shephard, M. W., Mlawer, E. J., Delamere, J. S., Iacono, M. J., Cady-Pereira, K., Boukabara, S., and Brown, P. D.: Atmospheric radiative transfer modeling: a summary of the AER codes, J. Quant. Spectrosc. Radiat. T., 91, 233–244, 2005.

Coheur, P.-F., Clarisse, L., Turquety, S., Hurtmans, D., and Clerbaux, C.: IASI measurements of reactive trace species in biomass burning plumes, Atmos. Chem. Phys., 9, 5655-5667, doi:10.5194/acp-9-5655-2009, 2009.

Dammers, E., Vigouroux, C., Palm, M., Mahieu, E., Warneke, T., Smale, D., Langerock, B., Franco, B., Van Damme, M., Schaap, M., Notholt, J., and Erisman, J. W.: Retrieval of ammonia from ground-based FTIR solar spectra, Atmos. Chem. Phys., 15, 12789-12803, doi:10.5194/acp-15-12789-2015, 2015.

Dammers, E., Palm, M., Van Damme, M., Vigouroux, C., Smale, D., Conway, S., Toon, G. C., Jones, N., Nussbaumer, E., Warneke, T., Petri, C., Clarisse, L., Clerbaux, C., Hermans, C., Lutsch, E., Strong, K., Hannigan, J. W., Nakajima, H., Morino, I., Herrera, B., Stremme, W., Grutter, M., Schaap, M., Wichink Kruit, R. J., Notholt, J., Coheur, P.-F., and Erisman, J. W.: An evaluation of IASI-NH3 with ground-based Fourier transform infrared spectroscopy measurements, Atmos. Chem. Phys., 16, 10351-10368, doi:10.5194/acp-16-10351-2016, 2016a.

Dammers, E., Palm, M., Van Damme, M., Shephard, M., Cady-Pereira, K., Capps, S., Clarisse, L., Coheur, P. and Erisman, J. W.: Validation of NH3 satellite observations by ground-based FTIR measurements, in EGU General Assembly Conference Abstracts, vol. 18, p. 1657., 2016b.

Dentener, F., Drevet, J., Lamarque, J. F., Bey, I., Eickhout, B., Fiore, A. M., Hauglustaine, D., Horowitz, L. W., Krol, M., Kulshrestha, U. C., Lawrence, M., Galy-Lacaux, C., Rast, S., Shindell, D., Stevenson, D., Van Noije, T., Atherton, C., Bell, N., Bergman, D., Butler, T., Cofala, J., Collins, B., Doherty, R., Ellingsen, K., Galloway, J., Gauss, M., Montanaro, V., Müller, J. F., Pitari, G., Rodriguez, J., Sanderson, M., Solmon, F., Strahan, S., Schultz, M., Sudo, K., Szopa, S. and Wild, O.: Nitrogen and sulfur deposition on regional and global scales: A multimodel evaluation, Global Biogeochem. Cycles, 20(4), doi:10.1029/2005GB002672, 2006.

Erisman, J. W., Bleeker, a., Galloway, J. and Sutton, M. S.: Reduced nitrogen in ecology and the environment, Environ. Pollut., 150(1), 140–149, doi:10.1016/j.envpol.2007.06.033, 2007.

Erisman, J.W., Sutton, M.A., Galloway, J., Klimont, Z. and Winiwarter, W., 2008. How a century of ammonia synthesis changed the world. Nature Geoscience, 1(10), pp.636-639.

Erisman, J. W., Galloway, J., Seitzinger, S., Bleeker, A. and Butterbach-Bahl, K.: Reactive nitrogen in the environment and its effect on climate change, Curr. Opin. Environ. Sustain., 3(5), 281–290, doi:10.1016/j.cosust.2011.08.012, 2011.

719   Farr, T. G., Rosen, P. a., Caro, E. and Crippen, R.: The Shuttle Radar Topography Mission, Rev. …, (2005), 1–
720   33, doi:10.1029/2005RG000183.1.INTRODUCTION, 2007.
721
722   Fowler, D., Coyle, M., Skiba, U., Sutton, M. A., Cape, J. N., Reis, S., Sheppard, L. J., Jenkins, A., Grizzetti, B.,
723   Galloway, J. N., Vitousek, P., Leach, A., Bouwman, A. F., Butterbach-Bahl, K., Dentener, F., Stevenson, D.,
724   Amann, M. and Voss, M.: The global nitrogen cycle in the twenty-first century, Philos. Trans. R. Soc. London B
725   Biol. Sci., 368(1621) [online] Available from:
726   http://rstb.royalsocietypublishing.org/content/368/1621/20130164.abstract, 2013.
727
728   Hase, F., Hannigan, J. W., Coffey, M. T., Goldman, a., Höpfner, M., Jones, N. B., Rinsland, C. P. and Wood, S.
729   W.: Intercomparison of retrieval codes used for the analysis of high-resolution, ground-based FTIR
730   measurements, J. Quant. Spectrosc. Radiat. Transf., 87(1), 25–52, doi:10.1016/j.jqsrt.2003.12.008, 2004.
731
732   Hase, F., Demoulin, P., Sauval, A. J., Toon, G. C., Bernath, P. F., Goldman, A., Hannigan, J. W., Rinsland, C.
733   P.: An empirical line-by-line model for the infrared solar transmittance spectrum from 700 to 5000 cm(-1), J.
734   Quant. Spectrosc. Ra., 102, 450–463, doi:10.1016/j.jqsrt.2006.02.026, 2006.
735
736   Heald, C. L., Collett Jr., J. L., Lee, T., Benedict, K. B., Schwandner, F. M., Li, Y., Clarisse, L., Hurtmans, D. R.,
737   Van Damme, M., Clerbaux, C., Coheur, P.-F., Philip, S., Martin, R. V., and Pye, H. O. T.: Atmospheric
738   ammonia and particulate inorganic nitrogen over the United States, Atmos. Chem. Phys., 12, 10295-10312,
739   doi:10.5194/acp-12-10295-2012, 2012
740
741   Holland, E. a., Dentener, F. J., Braswell, B. H. and Sulzman, J. M.: Contemporary and pre-industrial global
742   reactive nitrogen budgets, Biogeochemistry, 46(1-3), 7–43, doi:10.1007/BF01007572, 1999.
743
744   Leen, J. B., Yu, X. Y., Gupta, M., Baer, D. S., Hubbe, J. M., Kluzek, C. D., Tomlinson, J. M. and Hubbell, M.
745   R.: Fast in situ airborne measurement of ammonia using a mid-infrared off-axis ICOS spectrometer, Environ.
746   Sci. Technol., 47(18), 10446–10453, doi:10.1021/es401134u, 2013.
747
748   Lonsdale, C. R., Hegarty, J. D., Cady-Pereira, K., Alvarado, M. J., Henze, D. K., Turner, M. D., Capps, S. L.,
749   Nowak, J. B., Neuman, J. A., Middlebrook, A. M., Bahreini, R., Murphy, J. G., Markovic, M., VandenBoer, T.
750   C., Russell, L. M., and Scarino, A. J.: Modeling the Diurnal Variability of Agricultural Ammonia in Bakersfield,
751   California during CalNex, Atmos. Chem. Phys. Discuss., doi:10.5194/acp-2016-44, in review, 2016
752
753   Lutsch, E., Dammers, E., Conway, S. and Strong, K., 2016. Long-range transport of NH_3, CO, HCN, and C_2H_6
754   from the 2014 Canadian Wildfires. Geophysical Research Letters, 43(15), pp.8286-8297,
755   doi:10.1002/2016GL070114, 2016.
756
757   Miller, D. J., Sun, K., Tao, L., Khan, M. A., and Zondlo, M. A.: Open-path, quantum cascade-laser-based sensor
758   for high-resolution atmospheric ammonia measurements, Atmos. Meas. Tech., 7, 81-93, doi:10.5194/amt-7-81-
759   2014, 2014
760
761   Moncet, J.-L, X. Liu, H. Snell, J. Eluszkiewicz, Y. He, T. Kennelly, R. Lynch, S. Boukabara, A. Lipton, H.
762   Rieu-Isaacs, G. Uymin, and S. Zaccheo : Algorithm Theoretical Basis Document for the Cross-track Infrared
763   Sounder Environmental Data Records, AER Document Number: P1187-TR-I-08, Version 4.2, available at:
764   http://www.star.nesdis.noaa.gov/jpss/documents/ATBD/D0001-M01-S01-007_JPSS_ATBD_CrIMSS_B.pdf,
765   (last access date: 24 October 2015), 2005.
766
767   Moncet, J.-L, Uymin G., Lipton A. E., and Snell H. E.: Infrared radiance modeling by optimal spectral
768   sampling. J. Atmos. Sci., 65, 3917-3934, 2008.
769
770   Morgenstern, O., Zeng, G., Wood, S. W., Robinson, J., Smale, D., Paton-Walsh, C., Jones, N. B., and Griffith,
771   D. W. T.: Long-range correlations in Fourier transform infrared, satellite, and modeled CO in the Southern
772   Hemisphere, J. Geophys. Res., 117, D11301 doi:10.1029/2012JD017639, 2012.
773
774   Myhre, G., Shindell, D., Bréon, F.-M., Collins, W., Fuglestvedt, J., Huang, J., Koch, D., Lamarque, J.-F., Lee,
775   D., Mendoza, B., Nakajima, T., Robock, A., Stephens, G., Takemura, T., and Zhang, H.: Anthropogenic and
776   Natural Radiative Forcing, in: Climate Change 2013: The Physical Science Basis. Contribution of Working
777   Group I to the Fifth Assessment Report of the Intergovernmental Panel on Climate Change, edited by: Stocker,

778   T. F., Qin, D., Plattner, G.-K., Tignor, M., Allen, S. K., Boschung, J., Nauels, A., Xia, Y., Bex, V., and Midgley,
779   P. M., Cambridge University Press, Cambridge, United Kingdom and New York, NY, USA, 2013
780
781   Nowak, J. B., Neuman, J. A., Kozai, K., Huey, L. G., Tanner, D. J., Holloway, J. S., Ryerson, T. B., Frost, G. J.,
782   McKeen, S. A., and Fehsenfeld, F. C.: A chemical ionization mass spectrometry technique for airborne
783   measurements of ammonia, J. Geophys. Res.-Atmos., 112, D10S02, doi:10.1029/2006JD007589, 2007.
784
785   Nowak, J. B., Neuman, J. A., Bahreini, R., Brock, C. A., Middlebrook, A. M., Wollny, A. G., Holloway, J. S.,
786   Peischl, J., Ryerson, T. B., and Fehsenfeld, F. C.: Airborne observations of ammonia and ammonium nitrate
787   formation over Houston, Texas, J. Geophys. Res.-Atmos., 115, D22 304, doi:10.1029/ 2010JD014195, 2010.
788
789   Nowak, J. B., Neuman, J. A., Bahreini, R., Middlebrook, A. M., Holloway, J. S., McKeen, S. A., Parrish, D. D.,
790   Ryerson, T. B. and Trainer, M.: Ammonia sources in the California South Coast Air Basin and their impact on
791   ammonium nitrate formation, Geophys. Res. Lett., 39(7), 2012.
792
793   Oren, R., Ellsworth, D.S., Johnsen, K.H., Phillips, N., Ewers, B.E., Maier, C., Schäfer, K.V., McCarthy, H.,
794   Hendrey, G., McNulty, S.G. and Katul, G.G., 2001. Soil fertility limits carbon sequestration by forest
795   ecosystems in a CO2-enriched atmosphere. Nature, 411(6836), pp.469-472.
796
797   Pope III, C. A., Burnett, R. T., Thun, M. J., Calle, E. E., Krewski, D., Ito, K. and Thurston, G. D.: Lung cancer,
798   cardiopulmonary mortality, and long-term exposure to fine particulate air pollution, Jama, 287(9), 1132–1141,
799   2002.
800
801   Pope, III, C. A., Ezzati, M., and Dockery, D. W.: Fine-Particulate Air Pollution and Life Expectancy in the
802   United States, N. Engl. J. Med., 360, 376–386, doi:{10.1056/NEJMsa0805646}, 2009.
803
804   Pougatchev, N. S., Connor, B. J., & Rinsland, C. P. (1995). Infrared measurements of the ozone vertical
805   distribution above Kitt Peak. Journal of Geophysical Research: Atmospheres (1984–2012), 100(D8), 16689-
806   16697.
807
808   Puchalski, M. A., M. E. Sather, J. T. Walker, C. M. Lehmann, D. A. Gay, J. Mathew, and W. P. Robarge (2011),
809   Passive ammonia monitoring in the United States: Comparing three different sampling devices, J. Environ.
810   Monit., 13(11), 3156–3167, doi:10.1039/c1em10553a.
811
812   Reis, S., Pinder, R. W., Zhang, M., Lijie, G., and Sutton, M. A.: Reactive nitrogen in atmospheric emission
813   inventories, Atmos. Chem. Phys., 9, 7657-7677, doi:10.5194/acp-9-7657-2009, 2009
814
815   Rockstrom, J., Steffen, W., Noone, K., Persson, A., Chapin, F. S., Lambin, E. F., Lenton, T. M., Scheffer, M.,
816   Folke, C., Schellnhuber, H. J., Nykvist, B., de Wit, C. A., Hughes, T., van der Leeuw, S., Rodhe, H., Sorlin, S.,
817   Snyder, P. K., Costanza, R., Svedin, U., Falkenmark, M., Karlberg, L., Corell, R. W., Fabry, V. J., Hansen, J.,
818   Walker, B., Liverman, D., Richardson, K., Crutzen, P. and Foley, J. A.: A safe operating space for humanity,
819   Nature, 461(7263), 472–475 [online] Available from: http://dx.doi.org/10.1038/461472a, 2009.
820
821   Rodgers, C. D.: Inverse methods for atmospheric Sounding: Theory and Practice, World Sci., Hackensack, NJ,
822   2000.
823
824   Rodgers, C. D. and Connor, B. J.: Intercomparison of remote sounding instruments, J. Geophys. Res. Atmos.,
825   108(D3), n/a–n/a, doi:10.1029/2002JD002299, 2003.
826
827   Rodhe, Henning, Frank Dentener, and Michael Schulz. "The global distribution of acidifying wet deposition."
828   Environmental Science & Technology 36.20 (2002): 4382-4388.
829
830   Rothman, L. S., Gordon, I. E., Babikov, Y., Barbe, a., Chris Benner, D., Bernath, P. F., Birk, M., Bizzocchi, L.,
831   Boudon, V., Brown, L. R., Campargue, a., Chance, K., Cohen, E. a., Coudert, L. H., Devi, V. M., Drouin, B. J.,
832   Fayt, a., Flaud, J. M., Gamache, R. R., Harrison, J. J., Hartmann, J. M., Hill, C., Hodges, J. T., Jacquemart, D.,
833   Jolly, a., Lamouroux, J., Le Roy, R. J., Li, G., Long, D. a., Lyulin, O. M., Mackie, C. J., Massie, S. T.,
834   Mikhailenko, S., Müller, H. S. P., Naumenko, O. V., Nikitin, a. V., Orphal, J., Perevalov, V., Perrin, a.,
835   Polovtseva, E. R., Richard, C., Smith, M. a H., Starikova, E., Sung, K., Tashkun, S., Tennyson, J., Toon, G. C.,
836   Tyuterev, V. G. and Wagner, G.: The HITRAN2012 molecular spectroscopic database, J. Quant. Spectrosc.
837   Radiat. Transf., 130, 4–50, doi:10.1016/j.jqsrt.2013.07.002, 2013.

838
839 Schaap, M., van Loon, M., ten Brink, H. M., Dentener, F. J., and Builtjes, P. J. H.: Secondary inorganic aerosol
840 simulations for Europe with special attention to nitrate, Atmos. Chem. Phys., 4, 857-874, doi:10.5194/acp-4-
841 857-2004, 2004.

842
843 Schiferl, L. D., Heald, C. L., Nowak, J. B., Holloway, J. S., Neuman, J. A., Bahreini, R., Pollack, I. B., Ryerson,
844 T. B., Wiedinmyer, C., and Murphy, J. G.: An investigation of ammonia and inorganic particulate matter in
845 California during the CalNex campaign, J. Geophys. Res.-Atmos., 119, 1883–1902,
846 doi:10.1002/2013JD020765, 2014.

847
848 Schiferl, L. D., Heald, C. L., Van Damme, M., Clarisse, L., Clerbaux, C., Coheur, P.-F., Nowak, J. B., Neuman,
849 J. A., Herndon, S. C., Roscioli, J. R., and Eilerman, S. J.: Interannual variability of ammonia concentrations
850 over the United States: sources and implications, Atmos. Chem. Phys., 16, 12305-12328, doi:10.5194/acp-16-
851 12305-2016, 2016

852
853 Seinfeld, J. H. and Pandis, S. N.: Atmospheric Chemistry and Physics, John Wiley, Hoboken, NJ, 1988.

854
855 Shephard, M.W., Clough, S. A., Payne, V. H., Smith,W. L., Kireev, S., and Cady-Pereira, K. E.: Performance of
856 the line-by-line radiative transfer model (LBLRTM) for temperature and species retrievals: IASI case studies
857 from JAIVEx, Atmos. Chem. Phys., 9, 7397–7417, doi:10.5194/acp-9-7397-2009, 2009.

858
859 Shephard, M. W., Cady-Pereira, K. E., Luo, M., Henze, D. K., Pinder, R. W., Walker, J. T., Rinsland, C. P.,
860 Bash, J. O., Zhu, L., Payne, V. H., and Clarisse, L.: TES ammonia retrieval strategy and global observations of
861 the spatial and seasonal variability of ammonia, Atmos. Chem. Phys., 11, 10743-10763, doi:10.5194/acp-11-
862 10743-2011, 2011

863
864 Shephard, M. W. and Cady-Pereira, K. E.: Cross-track Infrared Sounder (CrIS) satellite observations of
865 tropospheric ammonia, Atmos. Meas. Techn., 8, 1323–1336, doi:10.5194/amt-8-1323-2015, http://www.
866 atmos-meas-tech.net/8/1323/2015/, 2015.

867
868 Shephard, M. W., McLinden, C. A., Cady-Pereira, K. E., Luo, M., Moussa, S. G., Leithead, A., Liggio, J.,
869 Staebler, R. M., Akingunola, A., Makar, P., Lehr, P., Zhang, J., Henze, D. K., Millet, D. B., Bash, J. O., Zhu, L.,
870 Wells, K. C., Capps, S. L., Chaliyakunnel, S., Gordon, M., Hayden, K., Brook, J. R., Wolde, M., and Li, S.-M.:
871 Tropospheric Emission Spectrometer (TES) satellite observations of ammonia, methanol, formic acid, and
872 carbon monoxide over the Canadian oil sands: validation and model evaluation, Atmos. Meas. Tech., 8, 5189-
873 5211, doi:10.5194/amt-8-5189-2015, 2015.

874
875 Sun, K., Cady-Pereira, K., Miller, D. J. , Tao, L., Zondlo, M.A. , Nowak, J. B., Neuman, J. A., Mikoviny, T.,
876 Müller, M. ,Wisthaler, A., Scarino, A. J., and Hostetler, C. A.: Validation of TES ammonia observations at the
877 single pixel scale in theSan Joaquin Valley during DISCOVER-AQ, J. Geophys. Res.-Atmos., 120, 5140–5154,
878 doi:10.1002/2014JD022846, 2015.

879
880
881 Sutton, M. a, Reis, S., Riddick, S. N., Dragosits, U., Nemitz, E., Theobald, M. R., Tang, Y. S., Braban, C. F.,
882 Vieno, M., Dore, A. J., Mitchell, R. F., Wanless, S., Daunt, F., Fowler, D., Blackall, T. D., Milford, C.,
883 Flechard, C. R., Loubet, B., Massad, R., Cellier, P., Personne, E., Coheur, P. F., Clarisse, L., Van Damme, M.,
884 Ngadi, Y., Clerbaux, C., Skjøth, C. A., Geels, C., Hertel, O., Wichink Kruit, R. J., Pinder, R. W., Bash, J. O.,
885 Walker, J. T., Simpson, D., Horváth, L., Misselbrook, T. H., Bleeker, A., Dentener, F. and de Vries, W.:
886 Towards a climate-dependent paradigm of ammonia emission and deposition., Philos. Trans. R. Soc. Lond. B.
887 Biol. Sci., 368(1621), 20130166, doi:10.1098/rstb.2013.0166, 2013.

888
889 Tobin, D.: Early Checkout of the Cross-track Infrared Sounder (CrIS) on Suomi-NPP, Through the
890 Atmosphere, Summer 2012, available at: www.ssec.wisc.edu/news/media/2012/07/ttasummer20121.pdf
891 (last access date: 30 January 2017), 2012.

892
893 Toon, G. C., Blavier, J.-F., Sen, B., Margitan, J. J., Webster, C. R., Max, R. D., Fahey, D. W., Gao, R.,
894 DelNegro, L., Proffitt, M., Elkins, J., Romashkin, P. A., Hurst, D. F., Oltmans, S., Atlas, E., Schauffler, S.,
895 Flocke, F., Bui, T. P., Stimpfle, R. M., Bonne, G. P., Voss, P. B., and Cohen, R. C.: Comparison of MkIV
896 balloon and ER-2 aircraft measurements of atmospheric trace gases, J. Geophys. Res., 104, 26 779–26 790,
897 1999.

898

899 Van Damme, M., Clarisse, L., Heald, C. L., Hurtmans, D., Ngadi, Y., Clerbaux, C., Dolman, A. J., Erisman, J.
900 W., and Coheur, P. F.: Global distributions, time series and error characterization of atmospheric ammonia
901 (NH3) from IASI satellite observations, Atmos. Chem. Phys., 14, 2905-2922, doi:10.5194/acp-14-2905-2014,
902 2014a.

903

904 Van Damme, M., R. J. Wichink Kruit, M. Schaap, L. Clarisse, C. Clerbaux, P.-F. Coheur, E. Dammers, A. J.
905 Dolman, and J. W. Erisman , Evaluating 4 years of atmospheric ammonia (NH3) over Europe using IASI
906 satellite observations and LOTOS-EUROS model results, J. Geophys. Res. Atmos., 119, 9549–9566,
907 doi:10.1002/2014JD021911, 2014b.

908

909 Van Damme, M., J. W. Erisman, L. Clarisse, E. Dammers, S. Whitburn, C. Clerbaux, A. J. Dolman, and P.-F.
910 Coheur (2015a), Worldwide spatiotemporal atmospheric ammonia (NH3) columns variability revealed by
911 satellite, Geophys. Res. Lett., 42, doi:10.1002/2015GL065496.

912

913 Van Damme, M., Clarisse, L., Dammers, E., Liu, X., Nowak, J. B., Clerbaux, C., Flechard, C. R., Galy-Lacaux,
914 C., Xu, W., Neuman, J. a., Tang, Y. S., Sutton, M. a., Erisman, J. W. and Coheur, P. F.: Towards validation of
915 ammonia (NH3) measurements from the IASI satellite, Atmos. Meas. Tech., 8(3), 1575–1591, doi:10.5194/amt-
916 8-1575-2015, 2015b.

917

918 Velazco, V., Wood, S. W., Sinnhuber, M., Kramer, I., Jones, N. B., Kasai, Y., Notholt, J., Warneke, T.,
919 Blumenstock, T., Hase, F., Murcray, F. J., and Schrems, O.: Annual variation of strato-mesospheric carbon
920 monoxide measured by ground-based Fourier transform infrared spectrometry, Atmos. Chem. Phys., 7, 1305-
921 1312, doi:10.5194/acp-7-1305-2007, 2007.

922

923 Warner, J. X., Wei, Z., Strow, L. L., Dickerson, R. R., and Nowak, J. B.: The global tropospheric ammonia
924 distribution as seen in the 13-year AIRS measurement record, Atmos. Chem. Phys., 16, 5467-5479,
925 doi:10.5194/acp-16-5467-2016, 2016

926

927 Whitburn, S., Van Damme, M., Kaiser, J. W., van der Werf, G. R., Turquety, S., Hurtmans, D., Clarisse, L.,
928 Clerbaux, C. and Coheur, P.-F.: Ammonia emissions in tropical biomass burning regions: Comparison between
929 satellite-derived emissions and bottom-up fire inventories, Atmos. Environ., 1–13,
930 doi:10.1016/j.atmosenv.2015.03.015, 2015.

931

932 Whitburn, S., M. Van Damme, L. Clarisse, S. Bauduin, C. L. Heald, J. Hadji-Lazaro, D. Hurtmans, M. A.
933 Zondlo, C. Clerbaux, and P.-F. Coheur (2016), A flexible and robust neural network IASI-NH3 retrieval
934 algorithm, J. Geophys. Res. Atmos., 121, 6581–6599, doi:10.1002/2016JD024828.

935

936 Wiacek, A., Taylor, J. R., Strong, K., Saari, R., Kerzenmacher, T. E., Jones, N. B. and Griffith, D. W. T.:
937 Ground-Based Solar Absorption FTIR Spectroscopy: Characterization of Retrievals and First Results from a
938 Novel Optical Design Instrument at a New NDACC Complementary Station, J. Atmos. Ocean. Technol., 24(3),
939 432–448, doi:10.1175/JTECH1962.1, 2007.

940

941 Worden, J., Kulawik S. S., Shephard M. W., Clough S. A., Worden H., Bowman K., and Goldman A.: Predicted
942 errors of tropospheric emission spectrometer nadir retrievals from spectral window selection, J. Geophys. Res.,
943 109, D09308, doi:10.1029/2004JD004522, 2004.

944

945

946 Zondlo, M., Pan, D., Golston, L., Sun, K. and Tao, L.: Ammonia emissions, transport, and deposition downwind
947 of agricultural areas at local to regional scales, in EGU General Assembly Conference Abstracts, vol. 18, p.
948 16552., 2016.

949

950 Zhu, L., Henze, D. K., Cady-Pereira, K. E., Shephard, M. W., Luo, M., Pinder, R. W., Bash, J. O. and Jeong, G.
951 R.: Constraining U.S. ammonia emissions using TES remote sensing observations and the GEOS-Chem adjoint
952 model, J. Geophys. Res. Atmos., 118(8), 3355–3368, doi:10.1002/jgrd.50166, 2013.

953